

1 Combined fluorescence, optical 2 diffraction tomography and Brillouin 3 microscopy

4 **Raimund Schlüßler^{1,*†}, Kyoohyun Kim^{1,2,*†}, Martin Nötzel¹, Anna
5 Taubenberger¹, Shada Abuhattum^{1,2}, Timon Beck^{1,2}, Paul Müller^{1,2},
6 Shovamayee Maharana¹, Gheorghe Cojoc¹, Salvatore Girardo^{1,2},
7 Andreas Hermann³, Simon Alberti^{1,4}, Jochen Guck^{1,2,4,*}**

*For correspondence:

raimund.schluessler@tu-dresden.de (RS);
kyoohyun.kim@mpl.mpg.de (KK);
jochen.guck@mpl.mpg.de (JG)

†These authors contributed
equally to this work

8 ¹Biotechnology Center, Center for Molecular and Cellular Bioengineering,
Technische Universität Dresden, 01307 Dresden, Germany; ²Max Planck
9 Institute for the Science of Light and Max-Planck-Zentrum für Physik und
10 Medizin, 91058 Erlangen, Germany; ³Translational Neurodegeneration
11 Section "Albrecht Kossel", University Rostock, and German Center for
12 Neurodegenerative Diseases (DZNE), Rostock/Greifswald, 18147 Rostock,
13 Germany; ⁴Physics of Life, Technische Universität Dresden, 01307
14 Dresden, Germany

17 **Abstract** Quantitative measurements of physical parameters become increasingly
18 important for understanding biological processes. Brillouin microscopy (BM) has
19 recently emerged as one technique providing the 3D distribution of viscoelastic
20 properties inside biological samples — so far relying on the implicit assumption that
21 refractive index (RI) and density can be neglected. Here, we present a novel method
22 (FOB microscopy) combining BM with optical diffraction tomography and
23 epi-fluorescence imaging for explicitly measuring the Brillouin shift, RI and absolute
24 density with molecular specificity. We show that neglecting the RI and density might
25 lead to erroneous conclusions. Investigating the cell nucleus, we find that it has lower
26 density but higher longitudinal modulus. Thus, the longitudinal modulus is not merely
27 sensitive to the water content of the sample — a postulate vividly discussed in the field.
28 We demonstrate the further utility of FOB on various biological systems including
29 adipocytes and intracellular membraneless compartments. FOB microscopy can
30 provide unexpected scientific discoveries and shed quantitative light on processes such
31 as phase separation and transition inside living cells.

33 Introduction

34 The mechanical properties of tissues, single cells, and intracellular compartments are
35 linked to their function, in particular during migration and differentiation, and as a re-

36 sponse to external stress (*Engler et al., 2006; Provenzano et al., 2006; Lo et al., 2000*).
37 Hence, characterizing mechanical properties *in vivo* has become important for under-
38 standing cell physiology and pathology, e.g. during development or cancer progression
39 (*Mammoto et al., 2013; Jansen et al., 2015; Mohammed et al., 2019*). To measure the
40 mechanical properties of biological samples, many techniques are available. These in-
41 clude atomic force microscopy (*Christ et al., 2010; Koser et al., 2015; Gautier et al., 2015;*
42 *Franze et al., 2013*), micropipette aspiration (*Maître et al., 2012*), and optical traps (*Wu*
43 *et al., 2018a; Litvinov et al., 2002; Bambardekar et al., 2015; Guck et al., 2001*). These
44 techniques can access the rheological properties of a sample and their changes under
45 various pathophysiological conditions. Yet, most of them require physical contact be-
46 tween probe and sample surface and none of them allows to obtain spatially resolved
47 distributions of the mechanical properties inside the specimens.

48 Brillouin microscopy has emerged as a novel microscopy technique to provide label-
49 free, non-contact, and spatially resolved measurements of the mechanical properties
50 inside biological samples (*Scarcelli and Yun, 2008; Scarcelli et al., 2015; Prevedel et al.,*
51 *2019*). The technique is based on Brillouin light scattering which arises from the inelas-
52 tic interaction between the incident photons and collective fluctuations of the molecules
53 (acoustic phonons) (*Brillouin, 1922; Boyd, 2008*). The Brillouin shift measured is related
54 to the longitudinal modulus, refractive index (RI), and absolute density of the sample
55 (see Methods). So far, conventional Brillouin microscopy does not consider the contri-
56 bution of heterogeneous RI and absolute density distributions to the longitudinal modu-
57 lus. Most studies either assume a homogeneous RI distribution (*Scarcelli and Yun, 2008;*
58 *Scarcelli et al., 2011; Antonacci and Braakman, 2016*), argument that the RI and absolute
59 density trivially cancel out (*Scarcelli et al., 2012, 2015; Antonacci et al., 2018*) or use RI
60 values obtained separately by other imaging setups (*Schlüßler et al., 2018*). Other ap-
61 proaches to calculate the longitudinal modulus measure the mass density of the sample,
62 but still rely on a priori knowledge of the RI (*Liu et al., 2019; Remer et al., 2020*). These
63 simplifications may result in an inaccurate calculation of the longitudinal modulus. Only
64 recently, serial Brillouin measurements of samples illuminated under different illumina-
65 tion angles allowed measuring the RI value inside the focal volume as well (*Fiore, 2019*).
66 However, this technique requires illuminating the sample from two different directions,
67 which doubles the acquisition time and decreases the spatial resolution of the measure-
68 ment when compared to a setup only acquiring the Brillouin shift.

69 Optical diffraction tomography (ODT) has been utilized for measuring the three-di-
70 mensional (3D) RI distribution of various specimens (*Sung et al., 2009; Cotte et al., 2013;*
71 *Kim et al., 2016*). Employing quantitative phase imaging, ODT can reconstruct the 3D
72 RI distribution of living biological samples from the complex optical fields measured un-
73 der different illumination angles. Given the RI, the mass density of most biological sam-
74 ples can be calculated using a two-substance mixture model (see Methods) (*Barer, 1952;*
75 *Popescu et al., 2008; Zangle and Teitell, 2014*). However, this requires knowledge of the
76 refraction increment, which depends on the material composition and takes on values of
77 0.173 ml/g to 0.215 ml/g with an average of 0.190 ml/g for different human proteins (*Zhao*
78 *et al., 2011; Theisen, 2000*) and can go down to 0.135 ml/g to 0.138 ml/g for phospholipids
79 (*Erbe and Sigel, 2007; Mashaghi et al., 2008*). Furthermore, the two-substance mixture
80 model does not apply to cell compartments mainly filled with a single substance, e.g.
81 lipid droplets in adipocytes. Hence, molecular specificity by e.g. fluorescence imaging is

82 necessary to determine whether the two-substance mixture model is appropriate and
83 which refraction increment should be used to calculate the absolute density of a certain
84 cell region.

85 Here, we present a combined optical system for epi-fluorescence, ODT, and Brillouin
86 microscopy (FOB microscopy) which can provide the correct longitudinal modulus from
87 colocalized measurements of the Brillouin shift and RI distributions and the subsequently
88 calculated absolute densities of a sample. The principal function of the FOB microscope is
89 demonstrated by measurements of cell phantoms made of biconstituent polymers with
90 known mechanical properties. We further applied the setup to HeLa cells and adipocytes.
91 First, we investigated two condensates that form by physical process of phase separation
92 – nucleoli in the nucleus and stress granules (SGs) in the cytoplasm (*Alberti and Dormann,*
93 *2019*). Nucleoli in HeLa cells showed a higher RI and longitudinal modulus than the cyto-
94 plasm, whereas the nucleoplasm had a lower RI than the cytoplasm while still showing a
95 higher longitudinal modulus. The RI of the cytoplasm and nucleoplasm decreased after
96 stressing HeLa cells with arsenite, but we found no significant difference of either the
97 RI or longitudinal modulus of SGs to the surrounding cytoplasm. By contrast, poly-Q ag-
98 gregates formed by overexpressing the aggregation-prone exon 1 of Q103 huntingtin ex-
99 hibited considerable differences to the surrounding compartment in terms of RI and lon-
100 gitudinal modulus. Moreover, unlike water-based cellular condensates and aggregates,
101 lipid droplets inside adipocytes showed higher RI and Brillouin shift, but lower longitudi-
102 nal modulus than the cytoplasm when taking into account their absolute density. These
103 data illustrates that in order to correctly calculate the longitudinal modulus, the RI as well
104 as the absolute density have to be taken into account. In summary, the presented setup
105 could provide measurement data necessary for a deeper understanding of pathophysi-
106 ological processes related to cell mechanics and condensates that form by the process
107 of phase separation.

108 Results

109 Optical setup

110 FOB microscopy combines ODT with Brillouin microscopy and epi-fluorescence imaging
111 (Fig. 1a). The three imaging modalities are sequentially applied to quantitatively map the
112 RI, the Brillouin shift, and the epi-fluorescence intensity distribution inside a given sample.
113 These parameters allow to e.g. infer the mass density and dry mass of the sample, and
114 provide molecular specificity for fluorescently labeled structures. Given the molecular
115 specificity, it is furthermore possible to localize subcellular organelles of interest and to
116 determine whether for a certain region the two-substance mixture model can be applied
117 to calculate the local absolute density, or if the literature value of the absolute density
118 has to be used (e.g. in lipid droplets). Finally, with the combination of RI, absolute density,
119 and Brillouin shift distributions, the longitudinal modulus can be calculated.

120 For ODT, the sample is illuminated with a plane wave under different incident angles.
121 To illuminate the sample under different angles, a dual-axis galvanometer mirror tilts the
122 illumination beam. The transmitted light interferes with a reference beam and creates a
123 spatially modulated hologram on a camera from which the phase delay and finally the RI
124 of the sample is calculated with a resolution of $0.25\ \mu\text{m}$ within the lateral plane and $0.5\ \mu\text{m}$
125 in the axial direction (Fig. 1c). Epi-fluorescence microscopy captures the fluorescence

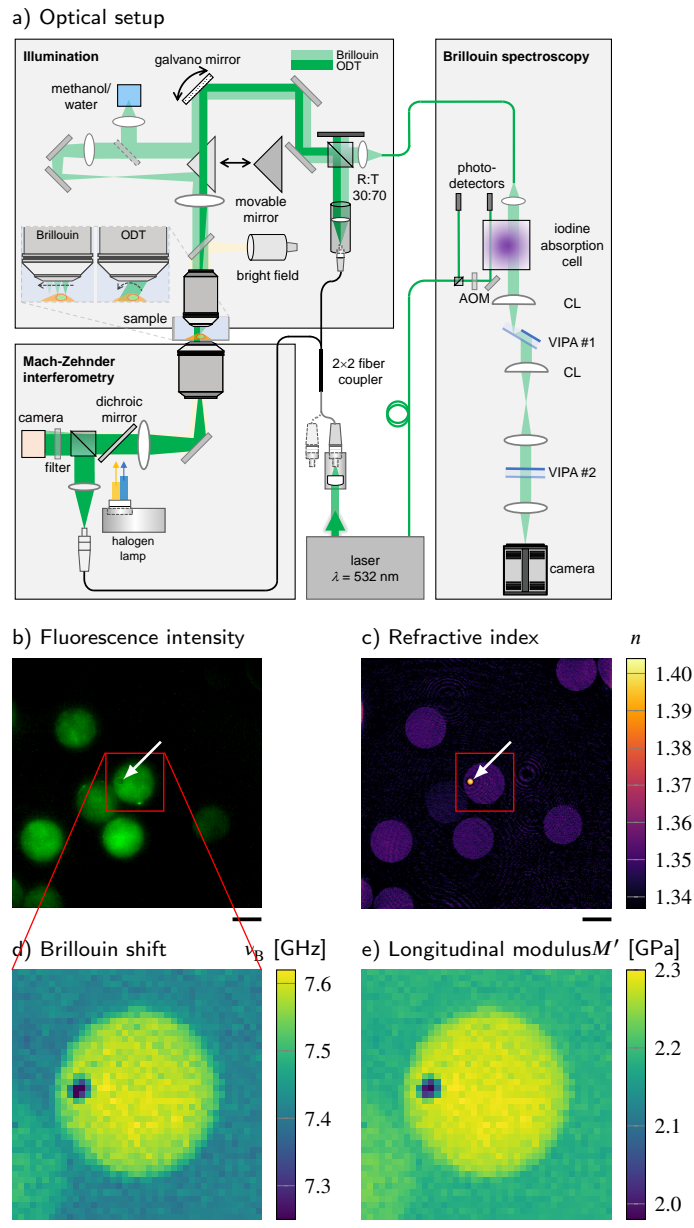


Figure 1. Combined fluorescence, optical diffraction tomography (ODT) and Brillouin microscopy. **(a)** Optical setup. The beam paths for epi-fluorescence / brightfield imaging, ODT and Brillouin microscopy are shown in light yellow, dark green and light green, respectively. The laser light illuminating the sample is collimated in ODT mode and focused in Brillouin mode. A moveable mirror enables to switch between the two modes. The Brillouin scattered light is guided to the spectrometer by a single-mode fiber, which acts as confocal pinhole. The light transmitted through the sample interferes with a reference beam. AOM, acousto-optic modulator; CL, cylindrical lens; LED, light-emitting diode; VIPA, virtually imaged phased array. **(b-e)** Quantitative and spatially resolved maps of a cell phantom consisting of a PDMS bead (indicated by the white arrows) inside a PAA bead stained with Alexa 488 (green fluorescence in **(b)**) acquired with the FOB microscope. **(b)** epi-fluorescence intensities, **(c)** refractive indices, **(d)** Brillouin shifts and **(e)** calculated longitudinal moduli. The size of the Brillouin map is 41 by 41 pixel, resulting in an acquisition duration of 30 min. Scale bars 10 μm .

126 emission intensity image (Fig. 1b) with the same camera used for the ODT acquisition.

127 For Brillouin microscopy, a moveable mirror guides the incident light to an additional
128 lens which leads to a focus in the sample with a size of $0.4\ \mu\text{m}$ in the lateral plane and
129 approximately $1\ \mu\text{m}$ in axial direction. The focus is translated by the galvanometer mirror
130 to scan the whole sample. The Brillouin scattered light is collected in the backscattering
131 configuration and guided to a two-stage virtually imaged phased array (VIPA) spectrom-
132 eter (*Scarcelli and Yun, 2008*). The Brillouin shift (Fig. 1d) is extracted from the recorded
133 Brillouin spectrum and the longitudinal modulus (Fig. 1e) is calculated from the Brillouin
134 shift, RI and absolute density distributions acquired (see Methods).

135 **Validation of the setup with cell phantoms**

136 To validate the basic performance of the combined FOB microscopy setup, we acquired
137 the RI and Brillouin shift of an artificial cell phantom with known material properties.
138 The phantom consists of a polydimethylsiloxane (PDMS) bead embedded in a polyacry-
139 lamide (PAA) bead (Fig. 1b-e) which was fluorescently labeled with Alexa 488 (See Meth-
140 ods). The RI of the embedded PDMS bead was measured as 1.3920 ± 0.0012 (mean value
141 \pm SEM) (Fig. 1c). This was slightly lower than values reported for bulk PDMS with the RI of
142 1.416 *Meichner et al. (2015)*, which could be due to the swelling of the PDMS beads dur-
143 ing the fabrication process *Wang et al. (2015)*. The RI of the PAA bead (1.3485 ± 0.0001)
144 was significantly lower than that of the PDMS bead, and was close to the previously
145 reported value *Girardo et al. (2018)*. In contrast, the Brillouin shift of the PDMS bead
146 (7.279 ± 0.019 GHz) was lower than for the PAA bead (7.574 ± 0.001 GHz) (Fig. 1d). In order to
147 calculate the longitudinal modulus, the absolute density of the PAA bead (1.0190 ± 0.0001 g/ml)
148 was calculated from the measured RI by applying a two-substance mixture model (See
149 Methods). However, this model cannot be applied for the PDMS bead, since the bead
150 does not contain a fluid phase. Hence, the area of the PDMS bead was segmented based
151 on the RI and fluorescence intensity (Fig. 1b), and the literature value for the absolute den-
152 sity of PDMS (1.03 g/ml) was used (see Supplementary Fig. 1) (*Rahman et al., 2012*). The
153 resulting longitudinal modulus is shown in Fig. 1e. We found values of 2.022 ± 0.013 GPa
154 for the PDMS bead and 2.274 ± 0.001 GPa for the PAA bead. The results are consistent
155 with previous measurements of the speed of sound in PDMS (*Cafarelli et al., 2017*) and
156 the longitudinal modulus of PAA (*Schlüßler et al., 2018*) when taking into account the ab-
157 solute density of the dry fraction (i.e. (2)). Our finding clearly demonstrates the strength
158 of the presented FOB setup to provide local RI and absolute density distributions for
159 correctly calculating longitudinal modulus from the Brillouin shift measured.

160 **Cell nucleoplasm has lower absolute density but higher longitudinal 161 modulus than cytoplasm**

162 The FOB microscope can also provide much needed quantitative insight into a biologi-
163 cal phenomenon that has recently captured the imagination of physicists and biologists
164 alike – the formation of membraneless compartments by liquid-liquid phase separation
165 (LLPS) (*Brangwynne et al., 2011*). One such membraneless compartment is the nucle-
166 olus, a region within the nucleus where ribosomal subunits are synthesized. Here, we
167 recorded the epi-fluorescence, Brillouin shift, and RI distributions of 139 HeLa cells in
168 which a nucleolar marker protein NIFK was tagged with GFP and the nuclei were stained
169 with Hoechst (See Methods). In order to evaluate the mechanical properties of the cyto-

170 plasm, nucleoplasm, and nucleoli separately, we segmented the different compartments
171 of the cells based on the RI and the two-channel epi-fluorescence intensity maps (Fig. 2a,
172 see Methods).

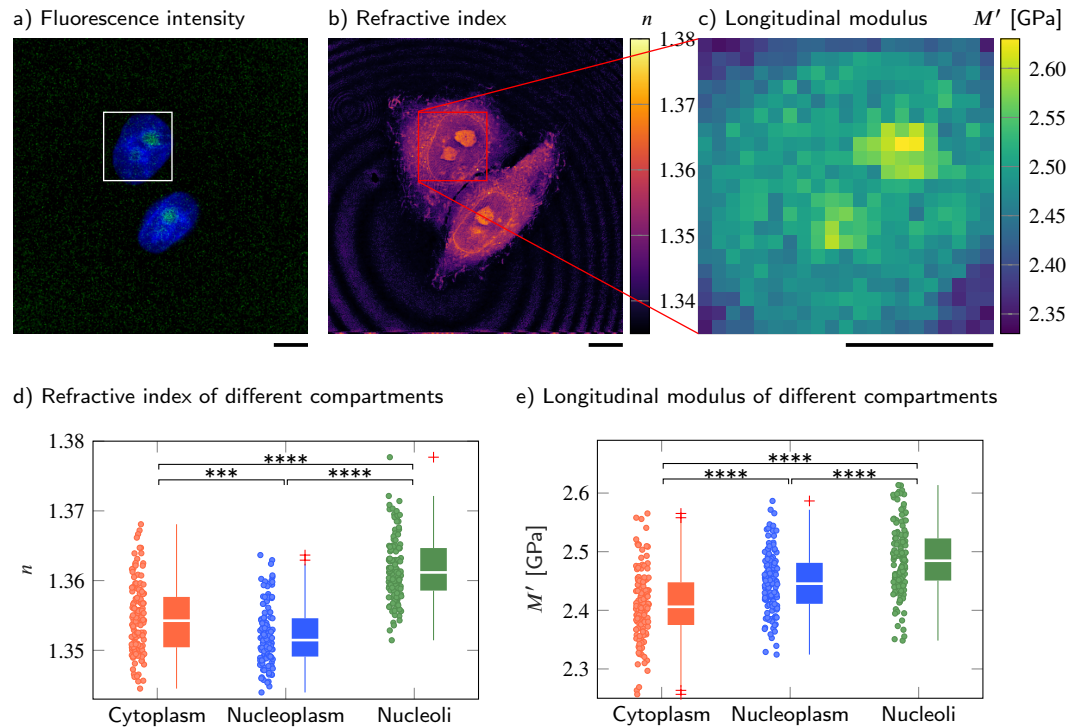


Figure 2. Cell nucleoplasm has lower RI but higher longitudinal modulus than cytoplasm. **(a-c)** Representative maps of the **(a)** epi-fluorescence intensity distribution, **(b)** longitudinal moduli and **(c)** refractive indices of a HeLa cell. Nuclei are stained with Hoechst (blue) and the nucleolar protein in the nucleoli is labeled with GFP (green). Quantitative analysis of **(d)** the refractive index and **(e)** the calculated longitudinal modulus taking into account the Brillouin shifts, refractive indices and absolute densities of 139 HeLa cells. The size of the Brillouin map is 21 by 21 pixel, resulting in an acquisition duration of 8 min. Scale bars 10 μm . *** $p < 0.001$; **** $p < 0.0001$.

173 As shown in Fig. 2b and d, the nucleoplasm of HeLa cells exhibited a significantly lower
174 RI than the cytoplasm (Kruskal-Wallis $p_{n_{\text{cyto}}, n_{\text{np}}} = 9 \times 10^{-4}$), with values of 1.3522 ± 0.0004 (nu-
175 cleoplasm) and 1.3545 ± 0.0004 (cytoplasm), which is consistent with previous studies (*Schür-*
176 *mann et al., 2016; Kim and Guck, 2020*). Since the RI of the HeLa cells measured is linearly
177 proportional to their mass density (*Kim and Guck, 2020*), we applied the two-substance
178 mixture model and used a global refraction increment of 0.190 ml/g, which is valid for pro-
179 tein and nucleic acid (*Zhao et al., 2011; Zangle and Teitell, 2014*), to calculate the absolute
180 densities of each cell and its compartments. The resulting absolute densities are shown
181 in Supplementary Fig. 2b. We found that the nucleoplasm had a lower absolute density
182 (1.0207 ± 0.0005 g/ml) than the cytoplasm (1.0234 ± 0.0006 g/ml). Here, the perinuclear cyto-
183 plasm also contains many lipid-rich membrane-bound organelles, and the RI increment
184 of phospholipids (0.135 ml/g to 0.138 ml/g, (*Erbe and Sigel, 2007; Mashaghi et al., 2008*))
185 is lower than that of protein and nucleic acid. Hence, the calculated absolute density
186 of the cytoplasm could be underestimated and the absolute density difference between
187 cytoplasm and nucleoplasm might be even more pronounced.

188 Interestingly, the Brillouin shift of the nucleoplasm (7.872 ± 0.007 GHz) was significantly
189 higher than the value of the cytoplasm (7.811 ± 0.008 GHz) ($p_{v_{B, \text{cyto}}, v_{B, \text{np}}} = 2 \times 10^{-6}$, Supple-
190 mentary Fig. 2a). The longitudinal moduli of the nucleoplasm (2.448 ± 0.005 GPa) and cy-
191 toplasm (2.410 ± 0.005 GPa) followed the same trend as the Brillouin shifts ($p_{M'_{\text{cyto}}, M'_{\text{np}}} =$
192 7×10^{-7} , Fig. 2c and e). Moreover, the nucleoli, where ribosomal subunits are synthesized,
193 exhibited significantly higher RI ($n = 1.3618 \pm 0.0004$), Brillouin shift ($v_b = 7.938 \pm 0.008$ GHz),
194 and longitudinal modulus ($M' = 2.487 \pm 0.005$ GPa) than either nucleoplasm or cytoplasm.
195 A full list of the resulting RI, Brillouin shifts, absolute densities and longitudinal moduli
196 and the corresponding p -values when comparing between different cell compartments
197 can be found in the Supplementary tables 1 and 2.

198 These findings imply that membraneless compartments formed by phase separation,
199 in this case the nucleolus, can maintain a higher absolute density and distinct compress-
200 ibility (here, higher longitudinal modulus) in spite of the thermodynamic instability inher-
201 ent in this state.

202 **PolyQ aggregates have higher absolute density and longitudinal mod-** 203 **ulus than cytoplasm**

204 To compare the properties of physiological condensates with a densely packed protein
205 aggregate, we overexpressed an expanded version of the aggregation-prone exon 1 of
206 huntingtin with 103 consecutive glutamines (*Lieberman et al., 2019; Norrbacka et al.,*
207 *2019; Bäuerlein et al., 2017*). Q103 phase separates into liquid droplets in cells and these
208 droplets rapidly convert into a solid-like state (*Yang and Yang, 2020*), meaning they do
209 not recover from photobleaching when subjected to fluorescence recovery after photo-
210 bleaching (FRAP) experiments (*Kroschwald et al., 2015*). Here, we observe polyglutamine
211 (polyQ) aggregates labeled with GFP in transiently transfected wild-type HeLa cells. We
212 used the FOB microscope to measure the mechanical properties of polyQ granules in
213 22 cells.

214 The polyQ aggregates showed a strong fluorescence signal in the GFP channel (Fig. 3a).
215 We hence used the fluorescence intensity to segment the aggregates from the peripheral
216 cytoplasm in order to quantitatively compare cytoplasm and aggregates (Fig. 3b and c).
217 The RI (1.3856 ± 0.0018) and the longitudinal modulus (3.051 ± 0.029 GPa) of the aggregates
218 were significantly higher ($p < 0.0001$) than the RI (1.3506 ± 0.0013) and longitudinal mod-
219 ulus (2.442 ± 0.009 GPa) of the peripheral cytoplasm (Fig. 3d and f and Supplementary
220 table 3). Our results show that FOB microscopy can quantify the physical properties of
221 cytoplasmic membraneless condensates – in principle.

222 **GFP-FUS stress granules in P525L HeLa cells show RI and longitudinal** 223 **modulus similar to the surrounding cytoplasm**

224 Recently, another type of condensates formed by LLPS — RNA and protein (RNP) gran-
225 ules, such as SGs — has received much attention, due to their linkage to neurodegener-
226 ative diseases such as amyotrophic lateral sclerosis (ALS) and frontotemporal dementia
227 (*Patel et al., 2015; Alberti and Hyman, 2016*). It is also increasingly recognized that the
228 mechanical properties of these compartments influence their functions and involvement
229 in disease (*Jawerth, 2018; Nötzel et al., 2018*). Fused in sarcoma (FUS) protein, an RNA-
230 binding protein involved in DNA repair and transcription, is one example of a protein
231 that localizes to SGs (*Patel et al., 2015*). Purified FUS protein is able to phase separate

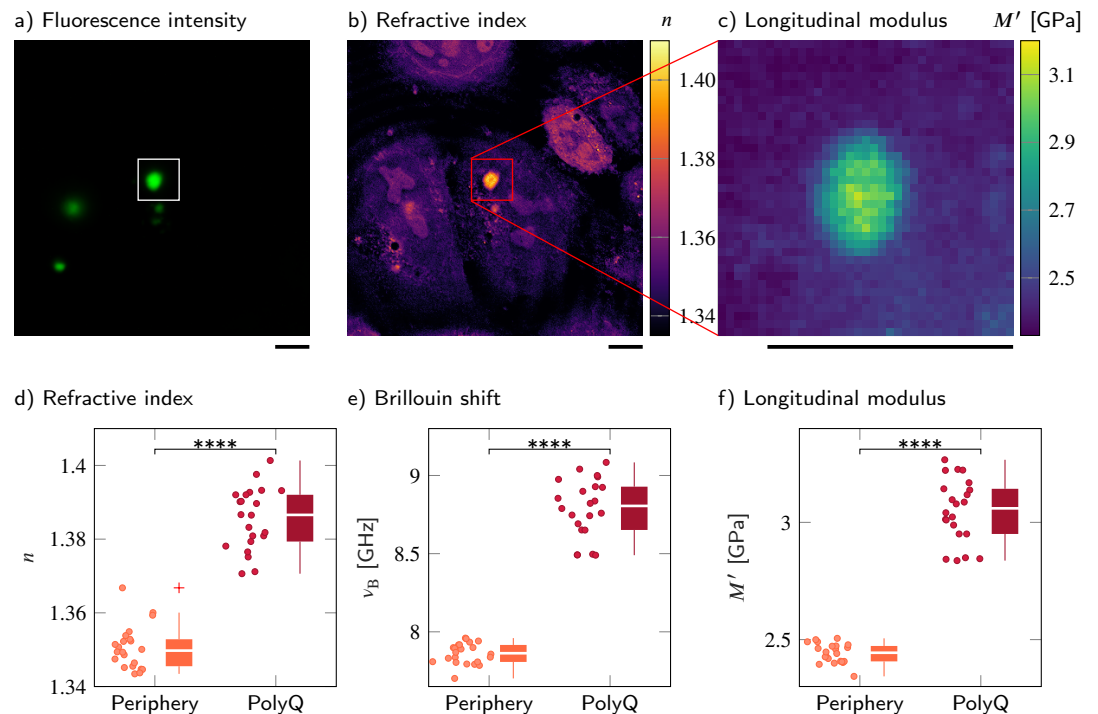


Figure 3. PolyQ aggregates have a higher refractive index, Brillouin shift and longitudinal modulus than the peripheral cytoplasm. **(a-c)** Representative maps of **(a)** the epi-fluorescence intensity distribution, **(b)** the refractive indices and **(c)** the longitudinal moduli of a HeLa cell transfected with a plasmid encoding HttQ103. The polyQ aggregates are labeled with GFP (green). Quantitative analysis of **(d)** the refractive index, **(e)** the Brillouin shift and **(f)** the calculated longitudinal modulus taking into account the Brillouin shifts, refractive indices and absolute densities of 22 polyQ granules. The size of the Brillouin map is 37 by 37 pixel, resulting in an acquisition duration of 23 min. Scale bars 10 μm. **** $p < 0.0001$.

232 into liquid condensates in vitro, and this property is important for FUS to localize to SGs.
233 Disease-linked mutations in FUS have been shown to promote a conversion of reconsti-
234 tuted liquid FUS droplets from a liquid to a solid state, suggesting that an aberrant liquid
235 to solid transition of FUS protein promotes disease.

236 Conventionally, the mechanical changes of SGs have been indirectly characterized by
237 FRAP or observing fusion events of liquid droplets (*Brangwynne et al., 2009*). Recently,
238 Brillouin microscopy was used to measure the Brillouin shift of SGs in chemically fixed
239 P525L HeLa cells expressing mutant RFP-tagged FUS under doxycycline exposure (*Ant-
240 tonacci et al., 2018*). P525L HeLa cells are used as a disease model for ALS and form
241 SGs under arsenite stress conditions. It was shown that the Brillouin shift of SGs induced
242 by arsenite treatment with mutant RFP-FUS is significantly higher than the Brillouin shift
243 of SGs without mutant RFP-FUS. Furthermore, the Brillouin shift of mutant RFP-FUS SGs
244 was reported to be significantly higher than the value of the surrounding cytoplasm (*Ant-
245 tonacci et al., 2018*).

246 Here, we applied the FOB setup to P525L HeLa cells which express GFP-tagged FUS,
247 and quantified the RI distributions, epi-fluorescence intensities, and Brillouin shifts of the
248 nucleoplasm, cytoplasm, and SGs. As not all HeLa cells were GFP-positive (see Fig. 4a), we
249 only selected the ones with a clear signal in the GFP channel. The cells were measured un-

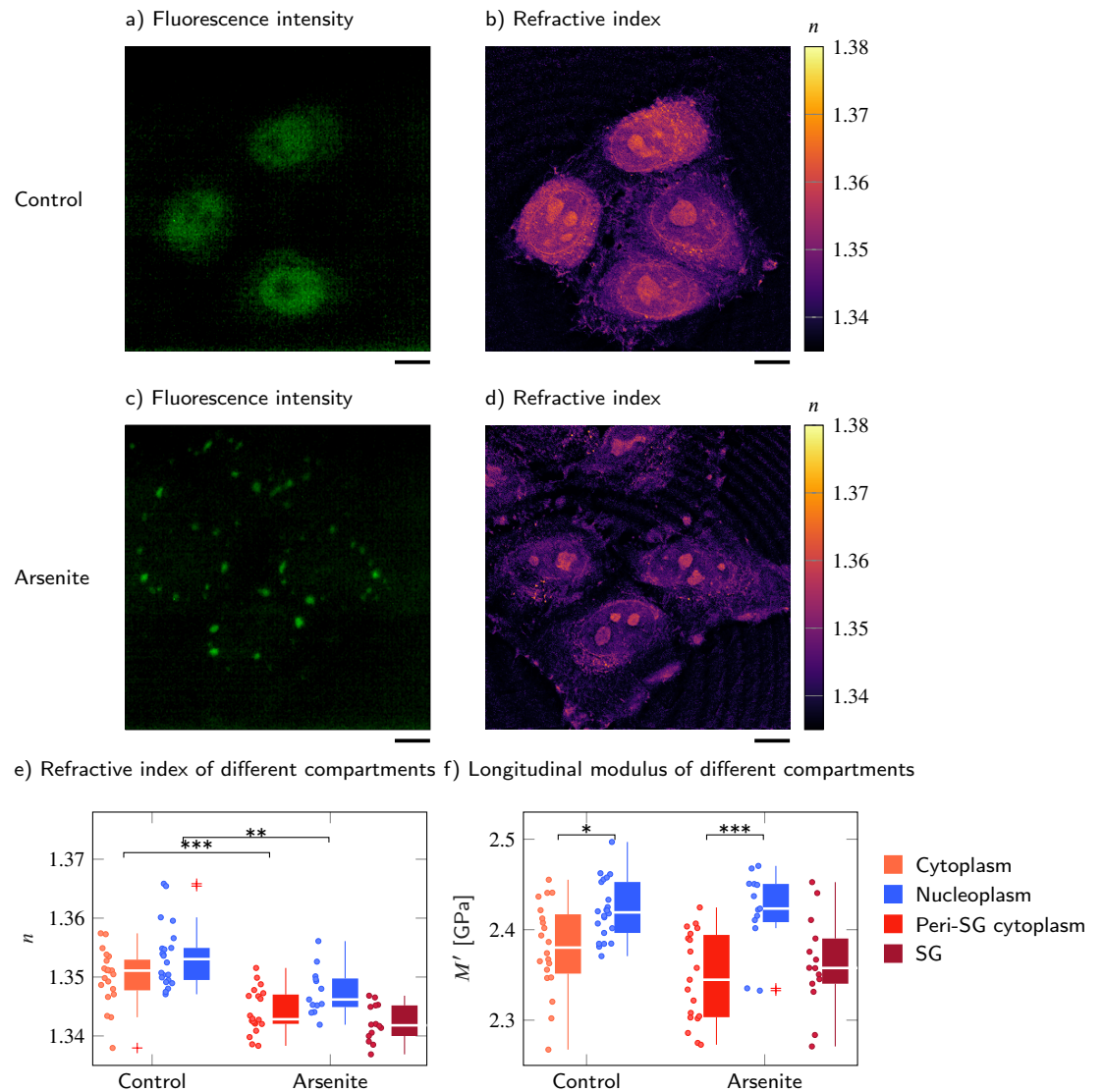


Figure 4. GFP-FUS-labelled stress granules induced by oxidative stress in P525L FUS HeLa cells show a similar RI and longitudinal modulus as the peripheral cytoplasm. Representative example of (a) the fluorescence intensity and (b) the refractive index distribution under control conditions without arsenite, and (c) the fluorescence intensity and (d) the refractive index distribution with arsenite. Quantitative analysis of (e) the refractive index and (f) the calculated longitudinal modulus taking into account the Brillouin shift and refractive index. * $p < 0.05$; ** $p < 0.01$; *** $p < 0.001$.

250 der control conditions or when exposed to 5 mM sodium arsenite NaAsO_2 30 min prior to
 251 the measurements. Since the SGs are not static, and assemble and disassemble dynami-
 252 cally, acquiring the Brillouin shift map of a complete cell would be too slow, which was the
 253 reason for fixing the cells in a previous study (Antonacci et al., 2018). During the approxi-
 254 mate duration of 20 min to 30 min of a whole cell measurement, SGs moved significantly
 255 or even disassembled and, hence, did not colocalize with their epi-fluorescence signal
 256 acquired before. Furthermore, the P525L GFP-FUS HeLa cells reacted sensitively to the
 257 exposure to green laser light and suffered from cell death during a whole cell measure-

258 ment. We therefore did not acquire a Brillouin shift map of the complete HeLa cells, but
259 only of a small region of $5\ \mu\text{m}$ by $5\ \mu\text{m}$ around the SGs or the corresponding region in the
260 cytoplasm of the control cells. This reduced the measurement duration to less than 2 min,
261 allowing us to colocalize the SGs Brillouin shift and epi-fluorescence signal and prevent-
262 ing cell death during the acquisition. The positions for the Brillouin shift measurements
263 of the different compartments were chosen manually based on the epi-fluorescence and
264 brightfield intensities (see Fig. 4a-d).

265 We found that, in difference to wild-type HeLa cells, the RI of the cytoplasm ($n_{\text{cyto}} =$
266 1.3500 ± 0.0010) and the RI of the nucleoplasm ($n_{\text{nucleo}} = 1.3535 \pm 0.0011$) were not signifi-
267 cantly different ($p > 0.05$) (Fig. 4e) and the RI of the nucleoplasm was even slightly higher
268 than the RI of the cytoplasm. However, when segmenting the RI of the whole cell and
269 not only taking into account the RI of the manually selected regions for which we also
270 performed measurements of the Brillouin shift, we found a slightly lower RI in the nucle-
271 oplasm ($n_{\text{nucleo,global}} = 1.3515 \pm 0.0004$) than in the cytoplasm ($n_{\text{cyto,global}} = 1.3521 \pm 0.0004$)
272 (Supplementary Fig. 3). Hence, we think the slightly higher RI of the nucleoplasm was an
273 artefact of the manual selection of the measurement positions. As for wild-type HeLa
274 cells, the longitudinal modulus of the nucleoplasm ($M'_{\text{nucleo}} = 2.421 \pm 0.007\ \text{GPa}$) was signif-
275 icantly higher than the modulus of the cytoplasm ($M'_{\text{cyto}} = 2.380 \pm 0.011\ \text{GPa}$, $p = 0.01$, Fig.
276 4f). While the GFP-tagged FUS of the control cells was mainly located in the nucleoplasm
277 (Fig. 4a), after arsenite treatment the FUS was relocated from the nucleoplasm and ag-
278 gregated in SGs within the cytoplasm (Fig. 4c). This was accompanied by a significant
279 decrease of the RI of both the peri-SG cytoplasm ($n_{\text{peri-cyto}} = 1.3442 \pm 0.0008$, $p = 0.0003$)
280 and the nucleoplasm ($n_{\text{nucleo}} = 1.3475 \pm 0.0011$, $p = 0.0054$). Even after the arsenite treat-
281 ment, there were no significant differences between the RI of the peri-SG cytoplasm
282 and the nucleoplasm ($p > 0.05$, Supplementary Fig. 3). Furthermore, we found no sig-
283 nificant difference of neither the RI ($n_{\text{SG}} = 1.3422 \pm 0.0008$) nor the longitudinal modulus
284 ($M'_{\text{SG}} = 2.362 \pm 0.014\ \text{GPa}$) of SGs to the respective values of the peri-SG cytoplasm. Al-
285 though the longitudinal modulus did not change significantly due to the arsenite treat-
286 ment, the difference between the longitudinal modulus of the peri-SG cytoplasm ($M'_{\text{cyto}} =$
287 $2.347 \pm 0.012\ \text{GPa}$) and the nucleoplasm ($M'_{\text{cyto}} = 2.421 \pm 0.012\ \text{GPa}$) was more pronounced
288 after the arsenite treatment ($p = 0.0001$, Fig. 4f).

289 Altogether, in P525L HeLa cells expressing GFP-FUS the RI of the cytoplasm and nucle-
290 oplasm showed no significant differences in untreated cells and decreased significantly
291 after arsenite treatment. For both the control and arsenite treated cells, the longitudinal
292 modulus of the nucleoplasm was significantly higher than the modulus of the cytoplasm
293 in terms of RI and longitudinal modulus. Interestingly, SGs showed no significant differ-
294 ences to the peri-SG cytoplasm. This is inconsistent to a previous study showing a higher
295 longitudinal modulus of SGs compared to cytoplasm (*Antonacci et al., 2018*). However, in
296 the previous study, a different cell line expressing RFP-tagged FUS was used, the sodium
297 arsenite concentration was lower (0.5 mM for 90 min vs. 5 mM for 30 min used here) and the
298 cells measured were chemically fixed. These differences might explain the discrepancy
299 of the results, especially since fixation can significantly alter the mechanical (*Braet et al.,*
300 *1998*) as well as the optical properties (*Su et al., 2014*) of biological samples.

301 **Mechanical characterization of lipid droplets in adipocytes requires** 302 **precise RI and density**

303 Most biological cells can be thought of as a mixture of ions and macromolecules such
304 as proteins, nucleic acids, and sugars dissolved in water, for which the two-substance
305 mixture model (*Barer, 1952; Popescu et al., 2008; Zangle and Teitell, 2014*) is appropriate
306 to describe the relationship between the RI and the absolute density. However, this is
307 not the case for special compartments in certain cell types. The lipid droplets within
308 adipocytes are not composed of a water-based solution and cannot be characterized by
309 the two-substance mixture model. To overcome this problem, we exploit the molecular
310 specificity of the FOB setup to identify and segment the lipid droplets. Since previous
311 mass spectroscopy studies on adipocyte cell culture models have identified palmitoyl
312 triacylglycerides as predominant lipid species (*Gouw and Vlugter, 1966; Liaw et al., 2016*),
313 we use an absolute density value of 0.8932 g/ml for calculating the longitudinal moduli of
314 the lipid droplets.

315 Here, we observed Simpson-Golabi-Behmel Syndrome (SGBS) adipocytes (*Wabitsch*
316 *et al., 2001*) ($N = 3$) whose nucleus and lipid droplets were stained with Hoechst and
317 Nile red respectively on day 11 of adipogenic differentiation. The lipid droplets were
318 clearly visible in the fluorescence intensity (Fig. 5a) and showed a high mean RI value of
319 1.409 ± 0.004 (Fig. 5c). The Brillouin shift of the lipid droplets of 8.25 ± 0.02 GHz was also sig-
320 nificantly higher than the Brillouin shift of the surrounding cytoplasm of 7.81 ± 0.02 GHz
321 (Fig. 5d). Hence, one could expect that the longitudinal modulus shows a similar trend as
322 the Brillouin shift as it does for samples described by the two-substance mixture model.
323 However, the longitudinal modulus of the lipid droplets (2.161 ± 0.005 GPa) was lower than
324 that of the cytoplasm (2.398 ± 0.009 GPa) when the measured RI and extracted absolute
325 density distributions were considered (Fig. 5e). The longitudinal modulus of lipid droplets
326 being lower than that of cytoplasm was consistent with previous measurement data of
327 the speed of sound of triacylglycerides which is lower than that of water (*Gouw and*
328 *Vlugter, 1967*). In order to demonstrate the effect of the RI and absolute density on the
329 calculation of the longitudinal modulus, we calculated the longitudinal modulus under
330 the assumption of a homogeneous RI (1.337) and absolute density (1 g/ml) distribution
331 instead of the values measured, as it would likely be done for a stand-alone Brillouin
332 microscope. The longitudinal modulus of lipid droplets without considering the RI and
333 absolute densities measured results to 2.717 ± 0.022 GPa, which was 26 % higher than the
334 correctly calculated longitudinal modulus (Fig. 5f). Our finding clearly demonstrates that
335 the local distribution of RI and absolute density can contribute considerably to the ex-
336 traction of the longitudinal modulus of the samples, especially for compartments which
337 cannot be described by the water-based two-substance mixture model.

338 **Discussion**

339 In this report, we experimentally demonstrated a combined epi-fluorescence, ODT, and
340 Brillouin (FOB) microscopy setup. The colocalized measurements and the subsequent
341 image analysis of the epi-fluorescence intensities and the RI distributions acquired by
342 the FOB setup allowed to identify regions of different material or molecular composi-
343 tion. This enabled us to extract the correct absolute density from either the RI measured
344 by applying the two-substance mixture model, or from the literature in case the two-

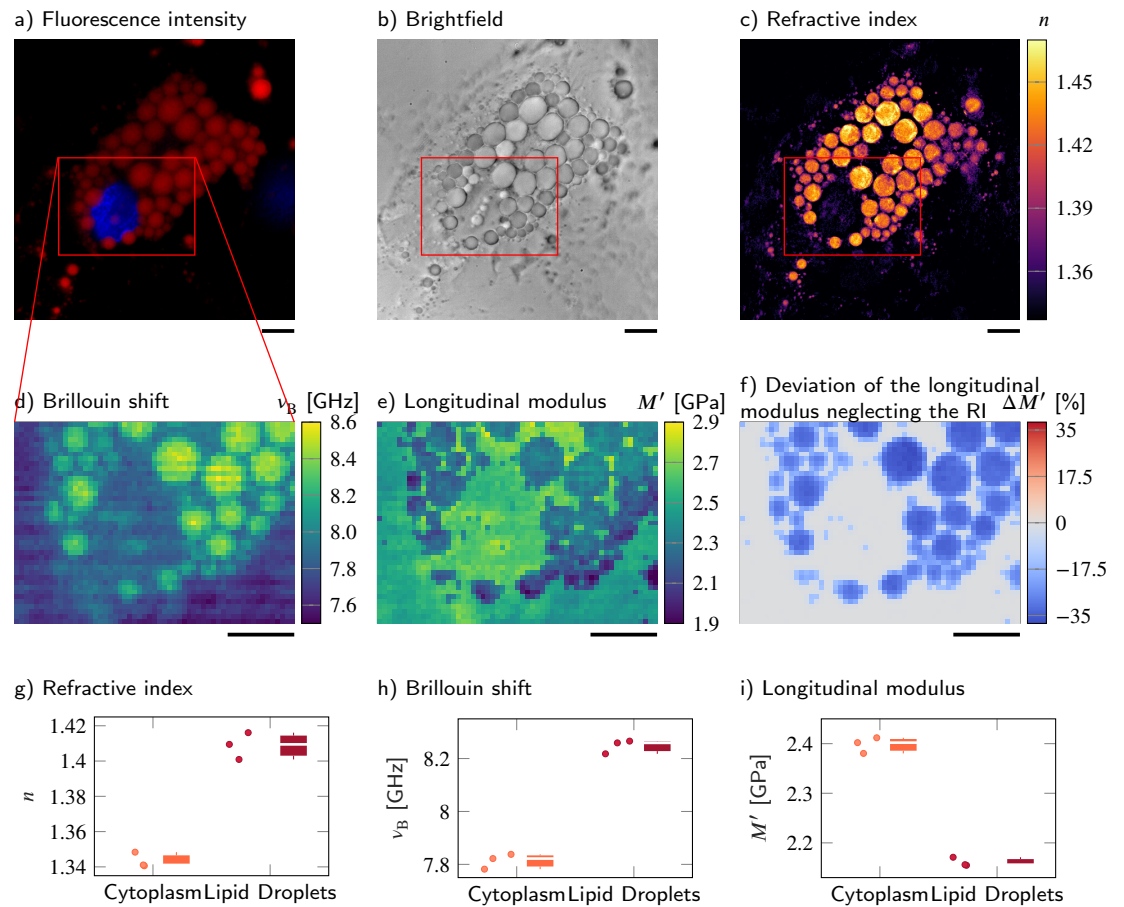


Figure 5. Despite a higher RI and Brillouin shift, the longitudinal modulus of lipid droplets is lower than of the surrounding cytoplasm. **(a-d)** Representative maps of the **(a)** epi-fluorescence intensities, **(b)** brightfield intensities, **(c)** refractive indices and **(d)** Brillouin shifts of an adipocyte cell. The nucleus is stained with Hoechst (blue in **(a)**) and lipid droplets are stained with Nile red (red in **(a)**). **(e)** Longitudinal modulus calculated from the refractive indices, absolute densities and Brillouin shifts. **(f)** Deviation of the longitudinal modulus calculated with a homogeneous refractive index and absolute density value when compared to the precise longitudinal modulus in **(e)**. Quantitative analysis of **(g)** the refractive index, **(h)** the Brillouin shift and **(i)** the calculated longitudinal modulus taking into account the Brillouin shifts, refractive indices and absolute densities of $N = 3$ adipocytes. The size of the Brillouin map is 57 by 41 pixel, resulting in an acquisition duration of 40 min. Scale bar 10 μm

345 substance mixture model is not applicable. In combination with the Brillouin shift dis-
 346 tributions measured, it was possible to accurately calculate the longitudinal moduli of a
 347 specimen. While in principle similar measurements would be possible with two separate
 348 setups individually acquiring Brillouin shift and RI, the combined setup simplifies sample
 349 handling, eliminates the necessity to locate the same cell or sample region on different
 350 setups and significantly reduces the time between the acquisition of the different modal-
 351 ities from multiple minutes to a few seconds. The last point is especially important for
 352 the analysis of dynamic processes such as the formation of SGs, which otherwise would
 353 not be captured adequately. We demonstrated the working principle of the setup using
 354 an artificial cell phantom consisting of a PDMS bead embedded in a PAA bead, for which

355 the acquired longitudinal moduli values are consistent with previous studies only when
356 we consider the RI and the absolute density of the PDMS and PAA bead.

357 The setup was also applied to investigate the physical and mechanical properties of
358 intracellular compartments in HeLa cells including nucleoplasm, cytoplasm, and nucle-
359 oli. We found that the nucleoplasm has a lower RI and absolute density than the cyto-
360 plasm while showing a higher Brillouin shift and longitudinal modulus. This is in line
361 with a previous publication reporting a higher Brillouin shift but lower mass density in
362 the chromatin network than in the cytoskeleton network of a mitotic macrophage-like
363 cell (*Liu et al., 2019*). Moreover, nucleoli, which are formed by liquid-liquid phase separa-
364 tion (LLPS) in the nucleoplasm, and polyQ aggregates, which undergo a rapid liquid-to-
365 solid transition in the cytoplasm, exhibit a significantly higher RI and longitudinal mod-
366 ulus than either nucleoplasm or cytoplasm. However, SGs in P525L HeLa cells, which
367 are also formed by LLPS, did not show significant differences in terms of RI or longitu-
368 dinal modulus compared to the surrounding cytoplasm. Hence, it seems that not every
369 condensation process is accompanied by changes of the RI, absolute density or longitu-
370 dinal modulus. Further investigation is required to reveal the underlying mechanism of
371 how nucleoli consisting of proteins and nucleic acids maintain a higher density and lon-
372 gitudinal modulus than the surrounding nucleoplasm despite the dynamic behavior of
373 compartments formed by LLPS (*Caragine et al., 2019*).

374 Currently, there is a vivid debate whether the Brillouin shift mainly depends on the
375 water content of the specimen, not on its mechanical properties (*Wu et al., 2018c,b; Scar-*
376 *celli and Yun, 2018; Bailey et al., 2019*). If we followed the idea that the water content
377 dominates the Brillouin shift, samples with a higher water content would exhibit a lower
378 Brillouin shift. As the RI of the cytoplasm and the nucleoplasm of the HeLa cells measured
379 here is linearly proportional to the mass density of macromolecules in water solution
380 (*Barer, 1952; Popescu et al., 2008*) and the refraction increments of both compartments
381 are similar (*Zhao et al., 2011; Zangle and Teitell, 2014*), the lower RI of the nucleoplasm
382 compared to the cytoplasm indicates that the nucleoplasm has a higher water content
383 than the cytoplasm. However, the nucleoplasm exhibits a higher Brillouin shift and lon-
384 gitudinal modulus than the surrounding cytoplasm. Hence, this result indicates that the
385 Brillouin shift and the longitudinal modulus are not only governed by the water content,
386 but are at least significantly influenced by the mechanical properties of the specimen.

387 An important aspect of the calculation of the longitudinal moduli is the extraction of
388 the densities of the samples. For samples or compartments that can be described by the
389 two-substance mixture model, we exploited the linear relation between the RI and the
390 mass density to calculate the absolute density value (*Barer, 1952; Popescu et al., 2008;*
391 *Zangle and Teitell, 2014*). However, as the partial specific volume of the dry fraction
392 is unknown, this approach might overestimate the absolute density by approximately
393 10% (see Methods). We find that in all samples measured here where the two-substance
394 mixture model can be applied, neglecting the contribution of RI and density to the longi-
395 tudinal modulus still yields a similar tendency for the longitudinal modulus and Brillouin
396 shift (i.e. a high Brillouin shift means a high longitudinal modulus and vice versa), but
397 doing so might lead to a systematic error for the longitudinal modulus. For cell com-
398 partments mainly containing a single substance, where this model cannot be applied,
399 e.g. lipid droplets in adipocytes, we used the molecular specificity provided by the epi-
400 fluorescence imaging to identify the respective regions and employed the literature value

401 for the absolute density in this region. Using this approach, we found that although the
402 RI and Brillouin shift of the lipid compartments in adipocytes are higher than those val-
403 ues of the cytoplasm, the resulting longitudinal modulus is actually lower when taking
404 into account the RI and absolute density distribution. This illustrates that RI and abso-
405 lute density do not cancel out for every cell and compartment – an implicit assumption
406 in many studies acquiring only the Brillouin shift – and that RI and absolute density have
407 to be known in order to precisely calculate the longitudinal modulus.

408 However, both the calculation of the absolute density from the RI and the identifica-
409 tion of regions not described by the two-substance mixture model rely on the knowledge
410 of the molecular composition of the sample. In order to calculate the absolute density
411 from the RI, the refraction increment has to be known, which, albeit comparable for pro-
412 teins and nucleic acids, might slightly vary between different cell compartments depend-
413 ing on their composition. Obviously, the composition also plays an important role when
414 selecting the correct literature value for the absolute density of compartments where
415 the two-substance mixture model is not applicable. As the molecular composition can-
416 not be resolved exactly by the FOB microscope, we used the refraction increment or
417 absolute density of the constituent likely predominant in a certain compartment. This
418 might lead to a slight deviation of the absolute density from the exact value, e.g. in the
419 membrane-rich perinuclear region of HeLa cells where the absolute density might be
420 underestimated. To overcome this issue and use the appropriate refraction increment
421 or absolute density for a mixture of different proteins, nucleic acids, or phospholipids,
422 more sophisticated labeling and staining of different molecules and the use of several
423 fluorescence channels might allow identifying multiple substances. Also, the absolute
424 concentration of different molecules could be directly measured from the intensity of
425 Raman scattering signals (*Oh et al., 2019*), an imaging extension that could be added for
426 future studies to the FOB setup presented here (*Traverso et al., 2015; Mattana et al.,*
427 *2018*).

428 Future improvements of the setup could include moving to a laser source with a
429 wavelength of 660 nm or higher to reduce cell damage due to phototoxicity (*Nikolić and*
430 *Scarcelli, 2019*). This would allow a higher laser power at the sample plane for Brillouin
431 microscopy, which reduces the acquisition time and could help analysing dynamic pro-
432 cesses. The implementation of tomogram reconstruction algorithms taking into account
433 multiple light scattering in the sample would further enable the setup to measure thick
434 tissues and organisms (*Lim et al., 2019; Chowdhury et al., 2019*).

435 In conclusion, the FOB setup allows a precise calculation of the longitudinal modulus
436 from the measured RI and Brillouin shift even for samples with a heterogeneous RI and
437 absolute density distribution. This enables quantitative measurements of the mechanical
438 properties of single cells and their compartments and could lead to a deeper understand-
439 ing of physiological and pathological processes such as phase separation and transition
440 in cells as a response to external stress.

441 **Methods**

442 **Optical setup**

443 The FOB microscope setup combines optical diffraction tomography (ODT), Brillouin mi-
444 croscopy and epi-fluorescence imaging in the same optical system. It allows to obtain

445 quantitative maps of the refractive indices (RI), the Brillouin shifts, and the fluorescence
446 and brightfield intensities of a sample.

447 In order to acquire the three-dimensional RI distribution, ODT employing Mach-Zehnder
448 interferometry is applied. Besides small modifications necessary for the combination
449 with Brillouin microscopy the ODT part of the setup is identical to the one presented in
450 *Abuhattum et al. (2018)*. As laser source a frequency-doubled Nd-YAG laser (Torus 532,
451 Laser Quantum Ltd, United Kingdom) with a wavelength of 532 nm and a maximum output
452 power of 750 mW is used for both ODT and Brillouin microscopy. The laser was chosen as
453 it offers a very low amplified spontaneous emission intensity of 110 dB necessary for Brillouin
454 measurements. The main beam of the laser is coupled into a single-mode fiber and
455 split into two beams by a 2×2 fiber coupler. One beam is used as the reference for the
456 Mach-Zehnder interferometer. The other beam is collimated and demagnified through a
457 tube lens with a focal length of 175 mm and a 40x/1.0 NA water dipping objective lens (Carl
458 Zeiss AG, Germany), and illuminates the sample in a custom-built inverted microscope.
459 To allow to reconstruct a three-dimensional RI tomogram of the sample, the sample is
460 illuminated under 150 different incident angles. The illumination angles are generated
461 by a dual-axis galvanometer mirror (GVS012/M, Thorlabs Inc., USA) which is placed at the
462 conjugate plane of the sample and diffracts the illumination beam. The diffracted beam
463 is collected by a 63x/1.2 NA water immersion objective lens (Carl Zeiss AG, Germany) and
464 a tube lens with a focal length of 200 mm. The sample and the reference beam then interfere
465 at the image plane of a CCD camera (FL3-U3-13Y3M-C, FLIR Systems Inc., USA) which
466 records the generated spatially modulated hologram of the sample. In some cases the
467 hologram additionally shows parasitic interference patterns originating from the protective
468 window in front of the CCD camera (see e.g. Fig. 2b. This is a general limitation of the
469 ODT setup, due to the coherent nature of the laser source). The setup achieves a spatial
470 resolution of $0.25 \mu\text{m}$ within the lateral plane and $0.5 \mu\text{m}$ in the axial direction.

471 In order to switch to Brillouin microscopy mode, a motorized mirror is moved into
472 the beam path guiding the light towards an additional lens with a focal length of 300 mm.
473 In combination with the upper tube lens this ensures a collimated beam before the microscope
474 objective and effectively creates a laser focus at the sample plane. Hence, in Brillouin
475 mode the galvanometer mirrors are located at the Fourier conjugate plane of the sample
476 and can move the laser focus in the sample plane (Fig. 1a, inset). This allows to scan the
477 laser focus over the sample by adjusting the galvanometer voltage. The relation between the
478 applied galvanometer voltage and the resulting focus position is calibrated by acquiring
479 images of the laser foci with the ODT camera and extracting the foci positions for different
480 galvanometer voltages. The Brillouin scattered light is collected in the backscattering
481 configuration with the same objective used for ODT and coupled into a single-mode fiber
482 which acts as a pinhole confocal to the illumination fiber and delivers the light to a two-stage
483 virtually imaged phased array (VIPA) Brillouin spectrometer (*Scarcelli and Yun, 2011*;
484 *Scarcelli et al., 2015*). This results in a spatial resolution of $0.4 \mu\text{m}$ within the lateral
485 plane and approximately $1 \mu\text{m}$ in the axial direction. In the spectrometer the beam is
486 collimated and passes through the iodine absorption cell, which blocks the Rayleigh
487 scattered and reflected light. The beam is then guided to two VIPA interferometers
488 (OP-6721-3371-2, Light Machinery, Canada) with 30 GHz free spectral range and a
489 spectral resolution of approximately $\delta\nu = 350 \text{ MHz}$, which is comparable to values
490 reported for other VIPA based setups (*Antonacci et al., 2013*) but lower than

491 the spectral resolution achievable with stimulated Brillouin scattering setups of around
492 100 MHz (Remer *et al.*, 2020). The Brillouin spectrum is imaged with an sCMOS camera
493 (Neo 5.5, Andor, USA) with a typical exposure time of 0.5 s at a laser power of 10 mW at
494 the sample.

495 Furthermore, the laser frequency is stabilized to the absorption maximum of a tran-
496 sition line of molecular iodine by controlling the laser cavity temperature. This allows to
497 attenuate the intensity of the Rayleigh scattered light entering the Brillouin spectrometer,
498 eliminates potential laser frequency drifts (Meng *et al.*, 2014; Schlüßler *et al.*, 2018) and
499 simplifies the mechanical alignment of the spectrometer as no masks for blocking the
500 elastically scattered light are necessary. To generate an error signal for the frequency
501 stabilization loop a small fraction of the laser light is frequency shifted by 350 MHz by
502 an acousto-optic modulator (AOM 3350-125, EQ Photonics GmbH, Germany) and guided
503 through an absorption cell (TG-ABI-Q, Precision Glass Blowing, USA) filled with iodine I₂.
504 The beam intensity is measured before and after the absorption cell by two photodetec-
505 tors (PDA36A2, Thorlabs Inc., USA) and a data acquisition card (PicoScope 2205A, Pico
506 Technology, United Kingdom). The quotient of both intensities is a measure for the ab-
507 sorption due to the iodine vapor. The laser cavity temperature is then controlled with
508 a custom C++ software LQTControl to achieve an absorption of 50 % for the frequency
509 shifted stabilization beam, which leads to maximum absorption for the not shifted main
510 beam.

511 To realise epi-fluorescence imaging, an incoherent beam from a white light halogen
512 lamp (DC-950, Dolan-Jenner Industries Inc., USA) is coupled into the setup by a three-
513 channel dichroic mirror (FF409/493/596-Di01-25x36, Semrock, USA). The bandwidth of
514 the excitation and emission beam is selected by two motorized filter sliders equipped
515 with band-pass filters in front of the halogen lamp and the CCD camera. A white light LED
516 (Thorlabs, USA) coupled into the Brillouin illumination path allows to observe a brightfield
517 image of the sample during Brillouin acquisition. Since fluorescence imaging and ODT
518 use the same objective, the acquired fluorescence images are guaranteed to focus the
519 central plane of the acquired RI tomogram.

520 The two cameras and all moveable optical devices of the setup are controlled with
521 a custom acquisition program written in C++. The software allows to control all three
522 imaging modalities and stores the acquired data as an HDF5 file.

523 **Refractive index tomogram reconstruction**

524 From the spatially modulated holograms recorded, the complex optical field of the light
525 scattered by the sample is retrieved by a field retrieval algorithm based on the Fourier
526 transform (CuChe *et al.*, 2000). The RI tomogram of the sample is reconstructed from
527 the retrieved optical fields with various incident angles via the Fourier diffraction theo-
528 rem. The detailed procedure for the tomogram reconstruction is presented in Kim *et al.*
529 (2014); Müller *et al.* (2016). The field retrieval and tomogram reconstruction were per-
530 formed by custom-made MATLAB (The MathWorks, Natick, USA) scripts. From the recon-
531 structed RI tomograms, subcellular compartments are segmented based on the RI and
532 epi-fluorescence signals. First, cell regions are segmented from background by apply-
533 ing the Otsu's thresholding method, and the watershed algorithm is used to determine
534 individual cells in the RI tomograms. Then, epi-fluorescence images of the fluorescence-
535 labeled subcellular compartments (e.g., nuclei, polyQ aggregates in HeLa cells, nuclei

536 and lipid droplets in adipocytes) are colocalized with the RI tomograms to segment the
537 compartments. In the nuclei of the HeLa cells, the RI tomogram regions having higher RI
538 values than surrounding nucleoplasm are segmented by the Otsu's thresholding method
539 and identified as nucleoli. The detailed segmentation procedure is described elsewhere
540 (*Schürmann et al., 2016; Kim and Guck, 2020*), and the source code for the segmentation
541 can be found at <https://github.com/OpticalDiffractionTomography/NucleiAnalysis>.

542 Brillouin shift evaluation

543 To evaluate the Brillouin shift ν_B , a custom MATLAB program is used. Details of the eval-
544 uation process can be found in *Schlüßler et al. (2018)*.

545 Calculation of the longitudinal modulus

546 The longitudinal modulus M' is determined by

$$M' = \rho \left(\frac{\lambda \nu_B}{2n \cos(\Theta/2)} \right)^2 \quad (1)$$

547 where the wavelength λ of the laser source and the scattering angle Θ are known param-
548 eters of the setup. The RI n and the Brillouin shift ν_B of the sample are measured using the
549 FOB microscope. The absolute density ρ can be calculated for the majority of biological
550 samples from the RI assuming a two-substance mixture. The absolute density is given
551 by (*Barer, 1952; Davies and Wilkins, 1952; Zangle and Teitell, 2014; Popescu et al., 2008;*
552 *Schlüßler et al., 2018*)

$$\rho = \frac{n - n_{\text{fluid}}}{\alpha} + \rho_{\text{fluid}} \cdot (1 - \rho_{\text{dry}} \cdot \bar{v}_{\text{dry}}) \quad (2)$$

553 with the RI n_{fluid} of the medium, the refraction increment α ($\alpha = 0.190 \text{ mL/g}$ for proteins
554 and nucleic acid (*Zhao et al., 2011; Zangle and Teitell, 2014; Biswas et al., 2021*)), the
555 absolute density ρ_{fluid} of the medium, the absolute density ρ_{dry} and the partial specific
556 volume \bar{v}_{dry} of the dry fraction. In case of $\rho_{\text{dry}} \ll \frac{1}{\bar{v}_{\text{dry}}}$ this can be simplified to

$$\rho \approx \frac{n - n_{\text{fluid}}}{\alpha} + \rho_{\text{fluid}} \quad (3)$$

557 This simplification leads to an overestimation of the absolute density and, hence, the lon-
558 gitudinal modulus, of around 10 % for e.g. HeLa cells, which we believe to be acceptable.

559 For certain cell types, e.g. adipocyte cells, the two-substance mixture model cannot be
560 applied for all cell compartments, i.e. the lipid droplets inside these cells do only consist
561 of lipids. Applying the two-substance model here leads to an unphysiological overesti-
562 mation of the absolute density. Hence, in special cases the absolute density cannot be
563 inferred from the RI and has to be estimated from the literature. This is possible with the
564 FOB microscope, since fluorescence labeling of the lipid droplets gives molecular speci-
565 ficity and allows to identify cell regions governed by e.g. lipids.

566 In order to calculate the longitudinal modulus and visualize the measurement results
567 of the FOB microscope, a custom MATLAB program FOBVisualizer is used. The software
568 allows to adjust the spatial alignment of the Brillouin and ODT measurements by cross-
569 correlating the two-dimensional maps acquired by both modalities and shifting the Brill-
570 ouin maps towards the highest correlation coefficient.

571 **Statistical analysis**

572 For the statistical analysis of the RI and longitudinal modulus differences between cyto-
573 plasm, nucleoplasm and nucleoli (Fig. 2 and Supplementary Fig. 2) the Kruskal-Wallis
574 test in combination with a least significant difference post-hoc test was used. The shown
575 asterisks indicate the significance levels: * $p < 0.05$, ** $p < 0.01$, *** $p < 0.001$ and **** $p <$
576 0.0001 . In box-and-whisker plots, the center lines indicate the medians, the edges of the
577 boxes define the 25th and 75th percentiles, the red plus signs represent data points out-
578 side the $\pm 2.7\sigma$ range which are considered outliers and the whiskers extend to the most
579 extreme data value that is not an outlier.

580 **Cell phantom preparation**

581 Artificial cell phantoms, consisting of polydimethylsiloxane (PDMS, Dow Corning Sylgard®
582 184) particles embedded in larger polyacrylamide microgel beads, were produced as fol-
583 low. The PDMS particles were generated by vortex-mixing a solution of 1 g PDMS (10:1
584 w/w, base/curing agent) dispersed in 10 ml of 2 % w/v poly(ethylene glycol) monooleate
585 (Merck Chemicals GmbH, Germany) aqueous solution. After mixing, the emulsion was
586 kept overnight in an oven at 75 °C to allow the polymerization of the PDMS droplets. The
587 size dispersion of the PDMS particle was reduced by centrifugation and removing all par-
588 ticles with a diameter larger than 5 μm . The final solution, containing PDMS particles with
589 a diameter lower than 5 μm , was washed three times in Tris-buffer (pH 7.48) and resus-
590 pended in 1 % w/v Pluronic® F-127 (Merck Chemicals GmbH, Germany) Tris-Buffer.

591 1 μl of concentrated PDMS particles were added to 100 μl polyacrylamide pre-gel mix-
592 ture with a total monomer concentration of 11.8 % w/v. This solution was used as a dis-
593 persed phase in a flow-focusing microfluidic device to produce PAAm microgel beads,
594 as previously described in *Girardo et al. (2018)*, embedding PDMS particles. N-hydroxy-
595 succinimide ester (0.1 % w/v, Merck Chemicals GmbH, Germany) was added to the oil
596 solution to functionalize the phantoms with Alexa 488. Precisely, 100 μl of Alexa Fluor™ hy-
597 drazide 488 (ThermoFisher Scientific, Germany) in deionized water (1 mg/ml) was added
598 to 100 μl phantom pellet and incubated overnight at 4 °C. The unbonded fluorophores
599 were removed by three washings in PBS. The final functionalized phantoms were stored
600 in PBS at 4 °C.

601 **Cell preparation**

602 The stable HeLa cell line expressing GFP fused to the N terminus of NIFK (Nucleolar pro-
603 tein interacting with the FHA domain of MKI67), was kindly provided by the lab of Anthony
604 Hyman (Max Planck Institute of Molecular Cell Biology and Genetics). The cells were cul-
605 tured in Dulbecco's modified Eagle's medium (DMEM) (31966-021, Thermo Fisher), high
606 glucose with GlutaMax medium (61965-026, Gibco) under standard conditions at 37 °C
607 and 5 % CO₂. The culture medium was supplemented with 10 % fetal bovine serum (FBS)
608 and 1 % penicillin-streptomycin. The cells were subcultured in a glass-bottom Petri dish
609 (FluoroDish, World Precision Instruments Germany GmbH) one day prior to the measure-
610 ment, and the culture medium was exchanged to Leibovitz's L-15 Medium without phenol
611 red (21083027, Thermo Fisher Scientific) prior to imaging. For staining nuclei, the cells
612 were stained with Hoechst (1:1000 dilution) for 10 min and washed with fresh Leibovitz's
613 L-15 medium prior to imaging.

614 The wild-type HeLa cells transiently expressing amyloid (Q103-GFP) aggregates were

615 cultured in DMEM (31966-021, Thermo Fisher), high glucose with GlutaMax medium (61965-
616 026, Gibco) under standard conditions at 37 °C and 5 % CO₂. The culture medium was
617 supplemented with 10 % fetal bovine serum (FBS) and 1 % penicillin-streptomycin. The
618 cells were subcultured in a glass-bottom Petri dish (FluoroDish, World Precision Instru-
619 ments Germany GmbH) two days prior to the measurement. One day prior to the mea-
620 surement the cells were transiently transfected with pcDNA3.1-Q103-GFP using Lipo-
621 factamine 2000 (Invitrogen, Carlsbad, California). Directly before the imaging the cul-
622 ture medium was exchanged to Leibovitz's L-15 Medium without phenol red (21083027,
623 Thermo Fisher Scientific).

624 The HeLa cells GFP-FUS WT (wild-type) and GFP-FUS^{P525L} (disease model for amy-
625 otrophic lateral sclerosis) were kindly provided by the lab of Anthony Hyman (Max Planck
626 Institute of Molecular Cell Biology and Genetics). The cells were cultured in 89 % DMEM
627 supplemented with 10 % FBS (Sigma-Aldrich; F7524) and 1 % penicillin-streptomycin under
628 standard conditions at 37 °C and 5 % CO₂. One day before the experiment the cells were
629 transferred to a 35 mm glass-bottom Petri dish (FluoroDish, World Precision Instruments
630 Germany GmbH). 30 min prior to the measurements the culture medium was exchanged
631 to Leibovitz's L-15 medium without phenol red (21083027, Thermo Fisher Scientific) and
632 the non-control samples were treated with 5 mM sodium arsenite.

633 **Adipocyte preparation**

634 Simpson-Golabi-Behmel Syndrome (SGBS) preadipocytes were cultured and differenti-
635 ated as described previously (*Wabitsch et al., 2001; Fischer-Posovszky et al., 2008*). For
636 regular cell culture, cells were maintained in Dulbecco's modified Eagles' Medium (DMEM)
637 / nutrient F-12 Ham (Thermofisher) supplemented with 4 μM panthotenic, 8 μM biotin
638 (Pan/Bio), 100 U/ml penicillin/100 μg/ml streptomycin (=OF-medium) with 10 % FBS (OF-
639 medium +FBS, Thermofisher) at 37 °C in T75 flasks. For adipogenic differentiation, cells
640 were washed with PBS, detached using TrypLE Express (Thermofisher) and seeded onto
641 glass-bottom Petri dishes (FluoroDish, World Precision Instruments Germany GmbH, 35 mm,
642 10⁵ cells). After 24 hours, cells were washed three times with serum-free OF-Medium,
643 and differentiation medium was added, consisting of OF-medium complemented with
644 10 μg/ml human transferrin (Sigma-Aldrich), 20 nM human insulin (Sigma-Aldrich), 2 μM
645 rosiglitazone (Cayman), 100 nM dexamethasone (Sigma-Aldrich), 250 μM 3-isobutyl-1-me-
646 thylxantine IBMX (Sigma-Aldrich), 100 nM cortisol (Sigma-Aldrich) and 0.2 nM triiodothyro-
647 nine T3 (Sigma-Aldrich). On day 4, the medium was exchanged to OF-medium supple-
648 mented with only transferrin, insulin, cortisol, T3 (concentrations as above). The medium
649 was replaced every fourth day. Cells were probed on day 11 of adipogenic differentiation.

650 **Code availability**

651 The source code of LQTControl, the program to stabilize the laser cavity temperature, is
652 open source and can be found on GitHub (<https://github.com/BrillouinMicroscopy/LQTControl>). The same is true for BrillouinAcquisition, the program for controlling and data
653 acquisition of the FOB microscope (<https://github.com/BrillouinMicroscopy/BrillouinAcquisition>), BrillouinEvaluation, used for evaluating Brillouin data (<https://github.com/BrillouinMicroscopy/BrillouinEvaluation>) and FOBVisualizer, used for viewing FOB microscop-
654 y data (<https://github.com/BrillouinMicroscopy/FOBVisualizer>). The Matlab scripts for
655 cell segmentation and ODT reconstruction can be found under <https://github.com/Op->
656
657
658

659 [ticalDiffractionTomography/NucleiAnalysis](#) and https://github.com/OpticalDiffractionTomography/ODT_Reconstruction, respectively.

661 **Data availability**

662 The data sets generated during and/or analyzed during the current study are available
663 from the corresponding author on reasonable request.

References

- 664
665 **Abuhattum S**, Kim K, Franzmann TM, Eßlinger A, Midtvedt D, Schlüßler R, Möllmert S, Kuan HS,
666 Alberti S, Ziburdaev V, Guck J. Intracellular Mass Density Increase Is Accompanying but Not
667 Sufficient for Stiffening and Growth Arrest of Yeast Cells. *Frontiers in Physics*. 2018; 6. doi:
668 [10.3389/fphy.2018.00131](https://doi.org/10.3389/fphy.2018.00131).
- 669 **Alberti S**, Dormann D. Liquid-Liquid Phase Separation in Disease. *Annual Review of Genetics*.
670 2019; 53(1):171–194. doi: [10.1146/annurev-genet-112618-043527](https://doi.org/10.1146/annurev-genet-112618-043527).
- 671 **Alberti S**, Hyman AA. Are Aberrant Phase Transitions a Driver of Cellular Aging? *BioEssays: News*
672 *and Reviews in Molecular, Cellular and Developmental Biology*. 2016 Oct; 38(10):959–968. doi:
673 [10.1002/bies.201600042](https://doi.org/10.1002/bies.201600042).
- 674 **Antonacci G**, Braakman S. Biomechanics of Subcellular Structures by Non-Invasive Brillouin Mi-
675 croscopy. *Scientific Reports*. 2016 Nov; 6(1):37217. doi: [10.1038/srep37217](https://doi.org/10.1038/srep37217).
- 676 **Antonacci G**, de Turreis V, Rosa A, Ruocco G. Background-Deflection Brillouin Microscopy Reveals
677 Altered Biomechanics of Intracellular Stress Granules by ALS Protein FUS. *Communications Bi-*
678 *ology*. 2018 Dec; 1(1):139. doi: [10.1038/s42003-018-0148-x](https://doi.org/10.1038/s42003-018-0148-x).
- 679 **Antonacci G**, Foreman MR, Paterson C, Török P. Spectral Broadening in Brillouin Imaging. *Applied*
680 *Physics Letters*. 2013 Nov; 103(22):221105. doi: [10.1063/1.4836477](https://doi.org/10.1063/1.4836477).
- 681 **Bailey M**, Alunni-Cardinali M, Correa N, Caponi S, Holsgrove T, Barr H, Stone N, Winlove CP,
682 Fioretto D, Palombo F. Brillouin-Derived Viscoelastic Parameters of Hydrogel Tissue Models.
683 arXiv:191208292 [cond-mat, physics:physics]. 2019 Dec; .
- 684 **Bambardekar K**, Clément R, Blanc O, Chardès C, Lenne PF. Direct Laser Manipulation Reveals the
685 Mechanics of Cell Contacts in Vivo. *Proceedings of the National Academy of Sciences*. 2015 Feb;
686 112(5):1416–1421. doi: [10.1073/pnas.1418732112](https://doi.org/10.1073/pnas.1418732112).
- 687 **Barer R**. Interference Microscopy and Mass Determination. *Nature*. 1952 Mar; 169(4296):366–367.
688 doi: [10.1038/169366b0](https://doi.org/10.1038/169366b0).
- 689 **Bäuerlein FJB**, Saha I, Mishra A, Kalemanov M, Martínez-Sánchez A, Klein R, Dudanova I, Hipp MS,
690 Hartl FU, Baumeister W, Fernández-Busnadiego R. In Situ Architecture and Cellular Interactions
691 of PolyQ Inclusions. *Cell*. 2017 Sep; 171(1):179–187.e10. doi: [10.1016/j.cell.2017.08.009](https://doi.org/10.1016/j.cell.2017.08.009).
- 692 **Biswas A**, Kim K, Cojoc G, Guck J, Reber S. The Xenopus Spindle Is as Dense as the Surrounding
693 Cytoplasm. *Developmental Cell*. 2021; .
- 694 **Boyd RW**. *Nonlinear Optics*. Academic Press; 2008.
- 695 **Braet F**, Rotsch C, Wisse E, Radmacher M. Comparison of Fixed and Living Liver Endothe-
696 lial Cells by Atomic Force Microscopy. *Applied Physics A*. 1998 Mar; 66(1):S575–S578. doi:
697 [10.1007/s003390051204](https://doi.org/10.1007/s003390051204).
- 698 **Brangwynne CP**, Eckmann CR, Courson DS, Rybarska A, Hoegge C, Gharakhani J, Jülicher F,
699 Hyman AA. Germline P Granules Are Liquid Droplets That Localize by Controlled Dissolu-
700 tion/Condensation. *Science*. 2009 Jun; 324(5935):1729–1732. doi: [10.1126/science.1172046](https://doi.org/10.1126/science.1172046).
- 701 **Brangwynne CP**, Mitchison TJ, Hyman AA. Active Liquid-like Behavior of Nucleoli Determines Their
702 Size and Shape in *Xenopus Laevis* Oocytes. *Proceedings of the National Academy of Sciences*.
703 2011 Mar; 108(11):4334–4339. doi: [10.1073/pnas.1017150108](https://doi.org/10.1073/pnas.1017150108).

- 704 **Brillouin L.** Diffusion de La Lumière et Des Rayons X Par Un Corps Transparent Homogène
705 - Influence de l'agitation Thermique. *Ann Phys.* 1922; 9(17):88–122. doi: 10.1051/an-
706 phys/192209170088.
- 707 **Cafarelli A, Verbeni A, Poliziani A, Dario P, Menciasci A, Ricotti L.** Tuning Acoustic and Mechanical
708 Properties of Materials for Ultrasound Phantoms and Smart Substrates for Cell Cultures. *Acta*
709 *Biomaterialia.* 2017 Feb; 49:368–378. doi: 10.1016/j.actbio.2016.11.049.
- 710 **Caragine CM, Haley SC, Zidovska A.** Nucleolar Dynamics and Interactions with Nucleoplasm in
711 Living Cells. *eLife.* 2019 Nov; 8:e47533. doi: 10.7554/eLife.47533.
- 712 **Chowdhury S, Chen M, Eckert R, Ren D, Wu F, Repina N, Waller L.** High-Resolution 3D Refrac-
713 tive Index Microscopy of Multiple-Scattering Samples from Intensity Images. *Optica.* 2019 Sep;
714 6(9):1211–1219. doi: 10.1364/OPTICA.6.001211.
- 715 **Christ AF, Franze K, Gautier H, Moshayedi P, Fawcett J, Franklin RJM, Karadottir RT, Guck J.**
716 Mechanical Difference between White and Gray Matter in the Rat Cerebellum Measured
717 by Scanning Force Microscopy. *Journal of Biomechanics.* 2010; 43(15):2986–2992. doi:
718 <http://dx.doi.org/10.1016/j.jbiomech.2010.07.002>.
- 719 **Cotte Y, Toy F, Jourdain P, Pavillon N, Boss D, Magistretti P, Marquet P, Depeursinge C.** Marker-Free
720 Phase Nanoscopy. *Nature Photonics.* 2013 Feb; 7(2):113–117. doi: 10.1038/nphoton.2012.329.
- 721 **Cuche E, Marquet P, Depeursinge C.** Spatial Filtering for Zero-Order and Twin-Image Elim-
722 ination in Digital off-Axis Holography. *Applied Optics.* 2000 Aug; 39(23):4070–4075. doi:
723 [10.1364/ao.39.004070](https://doi.org/10.1364/ao.39.004070).
- 724 **Davies HG, Wilkins MHF.** Interference Microscopy and Mass Determination. *Nature.* 1952 Mar;
725 169(4300):541–541. doi: 10.1038/169541a0.
- 726 **Engler AJ, Sen S, Sweeney HL, Discher DE.** Matrix Elasticity Directs Stem Cell Lineage Specification.
727 *Cell.* 2006 Aug; 126(4):677–689. doi: 10.1016/j.cell.2006.06.044.
- 728 **Erbe A, Sigel R.** Tilt Angle of Lipid Acyl Chains in Unilamellar Vesicles Determined by Ellipsometric
729 Light Scattering. *The European Physical Journal E, Soft Matter.* 2007 Apr; 22(4):303–309. doi:
730 [10.1140/epje/e2007-00038-5](https://doi.org/10.1140/epje/e2007-00038-5).
- 731 **Fiore A.** Direct Three-Dimensional Measurement of Refractive Index via Dual Photon-Phonon Scat-
732 tering. *Physical Review Letters.* 2019; 122(10). doi: 10.1103/PhysRevLett.122.103901.
- 733 **Fischer-Posovszky P, Newell FS, Wabitsch M, Tornqvist HE.** Human SGBS Cells - a Unique Tool for
734 Studies of Human Fat Cell Biology. *Obesity Facts.* 2008; 1(4):184–189. doi: 10.1159/000145784.
- 735 **Franze K, Janmey PA, Guck J.** Mechanics in Neuronal Development and Repair. *Annual Review of*
736 *Biomedical Engineering.* 2013; 15(1):227–251. doi: 10.1146/annurev-bioeng-071811-150045.
- 737 **Gautier HOB, Thompson AJ, Achouri S, Koser DE, Holtzmann K, Moendarbary E, Franze K.** Atomic
738 Force Microscopy-Based Force Measurements on Animal Cells and Tissues. In: *Methods in Cell*
739 *Biology*, vol. 125 Elsevier; 2015.p. 211–235. doi: 10.1016/bs.mcb.2014.10.005.
- 740 **Girardo S, Träber N, Wagner K, Cojoc G, Herold C, Goswami R, Schlüßler R, Abuhattum S, Tauben-
741 berger A, Reichel F, Mokbel D, Herbig M, Schürmann M, Müller P, Heida T, Jacobi A, Ulbricht E,
742 Thiele J, Werner C, Guck J.** Standardized Microgel Beads as Elastic Cell Mechanical Probes. *Journal*
743 *of Materials Chemistry B.* 2018 Sep; doi: 10.1039/C8TB01421C.
- 744 **Gouw IRT, Vlughter IRJC.** Physical Properties of Triglycerides III: Ultrasonic Sound Velocity. *Fette,*
745 *Seifen, Anstrichmittel.* 1967; 69(3):159–164. doi: 10.1002/lipi.19670690301.

- 746 **Gouw TH**, Vlugter JC. Physical Properties of Triglycerides. I. Density and Refractive Index. *Fette*,
747 *Seifen, Anstrichmittel*. 1966; 68(7):544–549. doi: [10.1002/lipi.19660680705](https://doi.org/10.1002/lipi.19660680705).
- 748 **Guck J**, Ananthakrishnan R, Mahmood H, Moon TJ, Cunningham CC, Käs J. The Optical Stretcher:
749 A Novel Laser Tool to Micromanipulate Cells. *Biophysical Journal*. 2001 Aug; 81(2):767–784. doi:
750 [10.1016/S0006-3495\(01\)75740-2](https://doi.org/10.1016/S0006-3495(01)75740-2).
- 751 **Jansen KA**, Donato DM, Balcioglu HE, Schmidt T, Danen EHJ, Koenderink GH. A Guide to Mechanobi-
752 ology: Where Biology and Physics Meet. *Biochimica et Biophysica Acta (BBA) - Molecular Cell*
753 *Research*. 2015 Nov; 1853(11, Part B):3043–3052. doi: [10.1016/j.bbamcr.2015.05.007](https://doi.org/10.1016/j.bbamcr.2015.05.007).
- 754 **Jawerth LM**. Salt-Dependent Rheology and Surface Tension of Protein Condensates Using Optical
755 Traps. *Physical Review Letters*. 2018; 121(25). doi: [10.1103/PhysRevLett.121.258101](https://doi.org/10.1103/PhysRevLett.121.258101).
- 756 **Kim K**, Guck J. The Relative Densities of Cytoplasm and Nuclear Compartments Are Robust against
757 Strong Perturbation. *Biophysical Journal*. 2020 Oct; doi: [10.1016/j.bpj.2020.08.044](https://doi.org/10.1016/j.bpj.2020.08.044).
- 758 **Kim K**, Yoon H, Diez-Silva M, Dao M, Dasari RR, Park Y. High-Resolution Three-Dimensional Imag-
759 ing of Red Blood Cells Parasitized by *Plasmodium Falciparum* and *in Situ* Hemozoin Crystals Us-
760 ing Optical Diffraction Tomography. *Journal of Biomedical Optics*. 2014; 19(1):011005. doi:
761 [10.1117/1.JBO.19.1.011005](https://doi.org/10.1117/1.JBO.19.1.011005).
- 762 **Kim K**, Yoon J, Shin S, Lee S, Yang SA, Park Y. Optical Diffraction Tomography Techniques for
763 the Study of Cell Pathophysiology. *Journal of Biomedical Photonics & Engineering*. 2016 Jun;
764 2(2):020201. doi: [10.18287/JBPE16.02.020201](https://doi.org/10.18287/JBPE16.02.020201).
- 765 **Koser DE**, Moeendarbary E, Hanne J, Kuerten S, Franze K. CNS Cell Distribution and Axon Ori-
766 entation Determine Local Spinal Cord Mechanical Properties. *Biophysical Journal*. 2015 May;
767 108(9):2137–2147. doi: [10.1016/j.bpj.2015.03.039](https://doi.org/10.1016/j.bpj.2015.03.039).
- 768 **Kroschwald S**, Maharana S, Mateju D, Malinowska L, Nüske E, Poser I, Richter D, Alberti S. Promis-
769 cuous Interactions and Protein Disaggregases Determine the Material State of Stress-Inducible
770 RNP Granules. *eLife*. 2015 Aug; 4:e06807. doi: [10.7554/eLife.06807](https://doi.org/10.7554/eLife.06807).
- 771 **Liaw L**, Prudovsky I, Koza RA, Anunciado-Koza RV, Siviski ME, Lindner V, Friesel RE, Rosen CJ, Baker
772 PRS, Simons B, Vary CPH. Lipid Profiling of In Vitro Cell Models of Adipogenic Differentiation:
773 Relationships With Mouse Adipose Tissues. *Journal of Cellular Biochemistry*. 2016; 117(9):2182–
774 2193. doi: [10.1002/jcb.25522](https://doi.org/10.1002/jcb.25522).
- 775 **Lieberman AP**, Shakkottai VG, Albin RL. Polyglutamine Repeats in Neurodegenerative Diseases.
776 *Annual Review of Pathology: Mechanisms of Disease*. 2019; 14(1):1–27. doi: [10.1146/annurev-
777 pathmechdis-012418-012857](https://doi.org/10.1146/annurev-pathmechdis-012418-012857).
- 778 **Lim J**, Ayoub AB, Antoine EE, Psaltis D. High-Fidelity Optical Diffraction Tomography of Multiple
779 Scattering Samples. *Light: Science & Applications*. 2019 Sep; 8(1):82. doi: [10.1038/s41377-019-
780 0195-1](https://doi.org/10.1038/s41377-019-0195-1).
- 781 **Litvinov RI**, Shuman H, Bennett JS, Weisel JW. Binding Strength and Activation State of Single
782 Fibrinogen-Integrin Pairs on Living Cells. *Proceedings of the National Academy of Sciences*. 2002
783 May; 99(11):7426–7431. doi: [10.1073/pnas.112194999](https://doi.org/10.1073/pnas.112194999).
- 784 **Liu L**, Plawinski L, Durrieu MC, Audoin B. Label-Free Multi-Parametric Imaging of Single Cells: Dual
785 Picosecond Optoacoustic Microscopy. *Journal of Biophotonics*. 2019; 12(8):e201900045. doi:
786 [10.1002/jbio.201900045](https://doi.org/10.1002/jbio.201900045).
- 787 **Lo CM**, Wang HB, Dembo M, Wang YL. Cell Movement Is Guided by the Rigidity of the Substrate.
788 *Biophysical Journal*. 2000 Jul; 79(1):144–152.

- 789 **Maître JL**, Berthoumieux H, Krens SFG, Salbreux G, Jülicher F, Paluch E, Heisenberg CP. Adhesion
790 Functions in Cell Sorting by Mechanically Coupling the Cortices of Adhering Cells. *Science*. 2012
791 Oct; 338(6104):253–256. doi: [10.1126/science.1225399](https://doi.org/10.1126/science.1225399).
- 792 **Mammoto T**, Mammoto A, Ingber DE. Mechanobiology and Developmental Control. *Annual Review*
793 *of Cell and Developmental Biology*. 2013; 29(1):27–61. doi: [10.1146/annurev-cellbio-101512-](https://doi.org/10.1146/annurev-cellbio-101512-122340)
794 [122340](https://doi.org/10.1146/annurev-cellbio-101512-122340).
- 795 **Mashaghi A**, Swann M, Popplewell J, Textor M, Reimhult E. Optical Anisotropy of Supported
796 Lipid Structures Probed by Waveguide Spectroscopy and Its Application to Study of Supported
797 Lipid Bilayer Formation Kinetics. *Analytical Chemistry*. 2008 May; 80(10):3666–3676. doi:
798 [10.1021/ac800027s](https://doi.org/10.1021/ac800027s).
- 799 **Mattana S**, Mattarelli M, Urbanelli L, Sagini K, Emiliani C, Serra MD, Fioretto D, Caponi S. Non-
800 Contact Mechanical and Chemical Analysis of Single Living Cells by Microspectroscopic Tech-
801 niques. *Light: Science & Applications*. 2018 Feb; 7(2):17139–17139. doi: [10.1038/lsa.2017.139](https://doi.org/10.1038/lsa.2017.139).
- 802 **Meichner C**, Schedl AE, Neuber C, Kreger K, Schmidt HW, Kador L. Refractive-Index Determination
803 of Solids from First- and Second-Order Critical Diffraction Angles of Periodic Surface Patterns.
804 *AIP Advances*. 2015 Aug; 5(8):087135. doi: [10.1063/1.4928654](https://doi.org/10.1063/1.4928654).
- 805 **Meng Z**, Traverso AJ, Yakovlev VV. Background Clean-up in Brillouin Microspectroscopy of Scatter-
806 ing Medium. *Optics Express*. 2014 Mar; 22(5):5410–5415. doi: [10.1364/OE.22.005410](https://doi.org/10.1364/OE.22.005410).
- 807 **Mohammed D**, Versaevel M, Bruyère C, Alaimo L, Luciano M, Vercruysse E, Procès A, Gabriele S.
808 Innovative Tools for Mechanobiology: Unraveling Outside-In and Inside-Out Mechanotransduc-
809 tion. *Frontiers in Bioengineering and Biotechnology*. 2019; 7. doi: [10.3389/fbioe.2019.00162](https://doi.org/10.3389/fbioe.2019.00162).
- 810 **Müller P**, Schürmann M, Guck J. The Theory of Diffraction Tomography. arXiv:150700466 [physics,
811 q-bio]. 2016 Oct; .
- 812 **Nikolić M**, Scarcelli G. Long-Term Brillouin Imaging of Live Cells with Reduced Absorption-Mediated
813 Damage at 660 Nm Wavelength. *Biomedical Optics Express*. 2019 Mar; 10(4):1567–1580. doi:
814 [10.1364/BOE.10.001567](https://doi.org/10.1364/BOE.10.001567).
- 815 **Norrbacka S**, Lindholm D, Myöhänen TT. Prolyl Oligopeptidase Inhibition Reduces PolyQ Aggre-
816 gation and Improves Cell Viability in Cellular Model of Huntington’s Disease. *Journal of Cellular*
817 *and Molecular Medicine*. 2019 Dec; 23(12):8511–8515. doi: [10.1111/jcmm.14675](https://doi.org/10.1111/jcmm.14675).
- 818 **Nötzel M**, Rosso G, Möllmert S, Seifert A, Schlüßler R, Kim K, Hermann A, Guck J. Axonal Trans-
819 port, Phase-Separated Compartments and Neuron Mechanics — a New Approach to Investigate
820 Neurodegenerative Diseases. *Frontiers in Cellular Neuroscience*. 2018; 12. doi: [10.3389/fn-](https://doi.org/10.3389/fn-12-00358)
821 [cel.2018.00358](https://doi.org/10.3389/fn-12-00358).
- 822 **Oh S**, Lee C, Yang W, Li A, Ran C, Yin W, Tabin CJ, Fu D, Xie XS, Kirschner MW. In Situ Measurement
823 of Absolute Concentrations by Normalized Raman Imaging. bioRxiv. 2019 May; p. 629543. doi:
824 [10.1101/629543](https://doi.org/10.1101/629543).
- 825 **Patel A**, Lee HO, Jawerth L, Maharana S, Jahnel M, Hein MY, Stoyanov S, Mahamid J, Saha S, Franz-
826 mann TM, Pozniakovski A, Poser I, Maghelli N, Royer LA, Weigert M, Myers EW, Grill S, Drechsel
827 D, Hyman AA, Alberti S. A Liquid-to-Solid Phase Transition of the ALS Protein FUS Accelerated by
828 Disease Mutation. *Cell*. 2015 Aug; 162(5):1066–1077. doi: [10.1016/j.cell.2015.07.047](https://doi.org/10.1016/j.cell.2015.07.047).
- 829 **Popescu G**, Park Y, Lue N, Best-Popescu C, Deflores L, Dasari RR, Feld MS, Badizadegan K. Optical
830 Imaging of Cell Mass and Growth Dynamics. *American Journal of Physiology - Cell Physiology*.
831 2008 Jun; 295(2):C538–C544.

- 832 **Prevedel R**, Diz-Muñoz A, Ruocco G, Antonacci G. Brillouin Microscopy: An Emerging Tool for
833 Mechanobiology. *Nature Methods*. 2019 Oct; 16(10):969–977. doi: 10.1038/s41592-019-0543-3.
- 834 **Provenzano PP**, Eliceiri KW, Campbell JM, Inman DR, White JG, Keely PJ. Collagen Reorganization
835 at the Tumor-Stromal Interface Facilitates Local Invasion. *BMC medicine*. 2006 Dec; 4(1):38. doi:
836 10.1186/1741-7015-4-38.
- 837 **Rahman MFA**, Arshad MR, Manaf AA, Yaacob MIH. An Investigation on the Behaviour of PDMS as
838 a Membrane Material for Underwater Acoustic Sensing. *IJMS Vol41(6) [December 2012]*. 2012
839 Dec; .
- 840 **Remer I**, Shaashoua R, Shemesh N, Ben-Zvi A, Bilenca A. High-Sensitivity and High-Specificity
841 Biomechanical Imaging by Stimulated Brillouin Scattering Microscopy. *Nature Methods*. 2020
842 Aug; 17(9):913–916. doi: 10.1038/s41592-020-0882-0.
- 843 **Scarcelli G**, Kim P, Yun SH. *In Vivo* Measurement of Age-Related Stiffening in the Crystalline
844 Lens by Brillouin Optical Microscopy. *Biophysical Journal*. 2011; 101(6):1539–1545. doi:
845 <http://dx.doi.org/10.1016/j.bpj.2011.08.008>.
- 846 **Scarcelli G**, Pineda R, Yun SH. Brillouin Optical Microscopy for Corneal Biomechanics. *Investigative*
847 *Ophthalmology & Visual Science*. 2012 Jan; 53(1):185–190. doi: 10.1167/iovs.11-8281.
- 848 **Scarcelli G**, Polacheck WJ, Nia HT, Patel K, Grodzinsky AJ, Kamm RD, Yun SH. Noncontact Three-
849 Dimensional Mapping of Intracellular Hydromechanical Properties by Brillouin Microscopy. *Nature*
850 *Methods*. 2015 Oct; 12:1132.
- 851 **Scarcelli G**, Yun SH. Confocal Brillouin Microscopy for Three-Dimensional Mechanical Imaging.
852 *Nature Photonics*. 2008 Jan; 2(1):39–43. doi: 10.1038/nphoton.2007.250.
- 853 **Scarcelli G**, Yun SH. Multistage VIPA Etalons for High-Extinction Parallel Brillouin Spectroscopy.
854 *Optics Express*. 2011 May; 19(11):10913–22.
- 855 **Scarcelli G**, Yun SH. Reply to ‘Water Content, Not Stiffness, Dominates Brillouin Spectroscopy
856 Measurements in Hydrated Materials’. *Nature Methods*. 2018 Aug; 15(8):562–563. doi:
857 10.1038/s41592-018-0075-2.
- 858 **Schlüßler R**, Möllmert S, Abuhattum S, Cojoc G, Müller P, Kim K, Möckel C, Zimmermann C, Czarske
859 J, Guck J. Mechanical Mapping of Spinal Cord Growth and Repair in Living Zebrafish Larvae by
860 Brillouin Imaging. *Biophysical Journal*. 2018 Aug; doi: 10.1016/j.bpj.2018.07.027.
- 861 **Schürmann M**, Scholze J, Müller P, Guck J, Chan CJ. Cell Nuclei Have Lower Refractive Index
862 and Mass Density than Cytoplasm. *Journal of Biophotonics*. 2016; 9(10):1068–1076. doi:
863 10.1002/jbio.201500273.
- 864 **Su JW**, Hsu WC, Tjiu JW, Chiang CP, Huang CW, Sung KB. Investigation of Influences of the
865 Paraformaldehyde Fixation and Paraffin Embedding Removal Process on Refractive Indices and
866 Scattering Properties of Epithelial Cells. *Journal of Biomedical Optics*. 2014 Jul; 19(7):075007. doi:
867 10.1117/1.JBO.19.7.075007.
- 868 **Sung Y**, Choi W, Fang-Yen C, Badizadegan K, Dasari RR, Feld MS. Optical Diffraction Tomog-
869 raphy for High Resolution Live Cell Imaging. *Optics Express*. 2009 Jan; 17(1):266–277. doi:
870 10.1364/OE.17.000266.
- 871 **Theisen A**. *Refractive Increment Data-Book for Polymer and Biomolecular Scientists*. Nottingham:
872 Nottingham University Press; 2000.

- 873 **Traverso AJ**, Thompson JV, Steelman ZA, Meng Z, Scully MO, Yakovlev VV. Dual Raman-Brillouin
874 Microscope for Chemical and Mechanical Characterization and Imaging. *Analytical Chemistry*.
875 2015 Aug; 87(15):7519–7523. doi: [10.1021/acs.analchem.5b02104](https://doi.org/10.1021/acs.analchem.5b02104).
- 876 **Wabitsch M**, Brenner R, Melzner I, Braun M, Möller P, Heinze E, Debatin KM, Hauner H. Charac-
877 terization of a Human Preadipocyte Cell Strain with High Capacity for Adipose Differentiation.
878 *International Journal of Obesity*. 2001 Jan; 25(1):8–15. doi: [10.1038/sj.ijo.0801520](https://doi.org/10.1038/sj.ijo.0801520).
- 879 **Wang C**, Moyses HW, Grier DG. Stimulus-Responsive Colloidal Sensors with Fast Holographic Read-
880 out. *Applied Physics Letters*. 2015 Aug; 107(5):051903. doi: [10.1063/1.4928178](https://doi.org/10.1063/1.4928178).
- 881 **Wu PH**, Aroush DRB, Asnacios A, Chen WC, Dokukin ME, Doss BL, Durand-Smet P, Ekpenyong A,
882 Guck J, Guz NV, Janmey PA, Lee JSH, Moore NM, Ott A, Poh YC, Ros R, Sander M, Sokolov I,
883 Staunton JR, Wang N, et al. A Comparison of Methods to Assess Cell Mechanical Properties.
884 *Nature Methods*. 2018 Jul; 15(7):491–498. doi: [10.1038/s41592-018-0015-1](https://doi.org/10.1038/s41592-018-0015-1).
- 885 **Wu PJ**, Kabakova I, Ruberti J, Sherwood JM, Dunlop IE, Paterson C, Török P, Overby DR. Brillouin Mi-
886 croscopy, What Is It Really Measuring? arXiv:171103312v2 [q-bioQM]. 2018; doi: [10.1038/s41592-018-0076-1](https://doi.org/10.1038/s41592-018-0076-1).
- 887
- 888 **Wu PJ**, Kabakova IV, Ruberti JW, Sherwood JM, Dunlop IE, Paterson C, Török P, Overby DR. Water
889 Content, Not Stiffness, Dominates Brillouin Spectroscopy Measurements in Hydrated Materials.
890 *Nature Methods*. 2018 Aug; 15(8):561–562. doi: [10.1038/s41592-018-0076-1](https://doi.org/10.1038/s41592-018-0076-1).
- 891 **Yang J**, Yang X. Phase Transition of Huntingtin: Factors and Pathological Relevance. *Frontiers in*
892 *Genetics*. 2020; 11. doi: [10.3389/fgene.2020.00754](https://doi.org/10.3389/fgene.2020.00754).
- 893 **Zangle TA**, Teitell MA. Live-Cell Mass Profiling: An Emerging Approach in Quantitative Biophysics.
894 *Nat Meth*. 2014 Dec; 11(12):1221–1228.
- 895 **Zhao H**, Brown PH, Schuck P. On the Distribution of Protein Refractive Index Increments. *Biophys-*
896 *ical Journal*. 2011 May; 100(9):2309–2317. doi: [10.1016/j.bpj.2011.03.004](https://doi.org/10.1016/j.bpj.2011.03.004).

897 **Acknowledgements**

898 We thank Anthony Hyman from the Max Planck Institute of Molecular Cell Biology and
899 Genetics for providing the stable HeLa cell lines, Prof. Martin Wabitsch from the Cen-
900 tre for Hormonal Disorders in Children and Adolescents – Ulm University Hospital for
901 providing the SGBS preadipocytes, and the Center for Molecular and Cellular Bioengi-
902 neering Light Microscopy Facility (partly funded by the State of Saxony and the European
903 Fund for Regional Development - EFRE) for technical support. Financial support from
904 the Deutsche Forschungsgemeinschaft (SPP 2191 – Molecular mechanisms of functional
905 phase separation, grant agreement number 419138906 to S.AI. and J.G.), Volkswagen
906 Stiftung (grant agreement number 92847 to S.AI. and J.G.), the Alexander von Humboldt-
907 Stiftung (Alexander von Humboldt-Professorship to J.G.) are gratefully acknowledged.
908 A.H. is supported by the NOMIS foundation and the Hermann und Lilly Schilling-Stiftung
909 für medizinische Forschung im Stifterverband.

910 **Author contributions statement**

911 R.S. evaluated the Brillouin measurements and wrote the software for the FOB micro-
912 scope. K.K. evaluated the refractive index measurements. K.K. and R.S. realized the FOB

013 microscope, conducted the FOB microscopy measurements and wrote the manuscript
014 with contributions from all authors. M.N. and R.S. cultured the P525L HeLa cells and
015 planned the respective experiment, S.M. helped with HeLa polyQ transfection. S.G. pro-
016 duced the phantom beads. S.Ab. and A.T. prepared the adipocyte cells. G.C., T.B. and
017 P.M. helped with the evaluation of the refractive index measurements. R.S., K.K., S.AI.
018 and J.G. designed the experiments. All authors reviewed the manuscript.

019 **Additional information**

020 **Competing financial interests** The authors declare no competing financial interests.